

Aus der Poliklinik für Zahnärztliche Prothetik
des Zentrums für Zahn-, Mund- und Kiefergesundheit
der Universität Würzburg

Direktor: Professor Dr. med. dent. Marc Schmitter

**Basic Dental Analytical Tools for a Comparative Study
of Applied Photoacoustics,
Cone-Beam Computed Tomography,
and Micro-Computed Tomography**

**Inauguraldissertation
zur Erlangung der Doktorwürde**

**der Medizinischen Fakultät
der Julius-Maximilians-Universität Würzburg**

vorgelegt von
Sonja Jasmin Maria Schneider
aus Tübingen

Würzburg, Dezember 2020

Referentenblatt

Referent: Prof. Dr. Marc Schmitter

Korreferent: Prof. Dr. Ulrich Schlagenhauf

Dekan: Prof. Dr. Matthias Frosch

Tag der mündlichen Prüfung:

24.5.2022

Die Promovendin ist Zahnärztin

To my parents

Contents

1	Introduction	1
1.1	Structure of Teeth	4
1.1.1	Enamel	5
1.1.1.1	Chemical Structure.....	5
1.1.1.2	Histological Structure	5
1.1.2	Dentin	6
1.1.2.1	Chemical Structure.....	6
1.1.2.2	Histological Structure	6
1.1.3	Pulp	7
1.1.4	Optical Properties of Dentin and Enamel.....	8
1.1.4.1	Refractive Index	8
1.1.4.1.1	Refractive Index of Enamel.....	9
1.1.4.1.2	Refractive Index of Dentin.....	9
1.1.5	Acoustic Properties of Dentin and Enamel	9
1.2	State-of-the-Art Imaging Techniques	10
1.2.1	Ionizing Imaging Techniques	11
1.2.1.1	Computed Tomography (CT)	11
1.2.1.2	Cone-Beam Computed Tomography (CBCT)	12
1.2.2	Non-Ionizing Imaging Techniques	12
1.2.2.1	Ultrasound (US)	13
1.2.2.2	Magnetic Resonance Imaging (MRI).....	14
1.2.2.3	Optical Coherence Tomography (OCT)	15
1.2.2.4	Photoacoustic Tomography (PAT)	15
1.3	Aim of the Present Study: Hypothesis.....	19
2	Materials and Methods.....	21

2.1	Preliminary Experiments	21
2.1.1	Teeth	21
2.1.2	Experimental Setup: Micro-Computed Tomography (μ -CT).....	21
2.1.3	Experimental Setup: Photoacoustic Tomography (PAT).....	24
2.1.4	Results of the Preliminary Experiment.....	27
2.2	Experimental Setup of the Main Study	27
2.2.1	Teeth	27
2.2.2	Experimental Setup: Micro-Computed Tomography (μ -CT).....	27
2.2.3	Experimental Setup: Cone-Beam Computed Tomography (CBCT) 28	
2.2.4	Experimental Setup: Photoacoustic Tomography (PAT).....	30
2.2.5	Data Analysis.....	32
2.2.6	Statistical Evaluation.....	37
2.2.6.1	Frequency Distribution	37
2.2.6.2	Significance Test.....	37
3	Results	38
3.1	Total Volume Comparisons: Micro-Computed Tomography vs. Cone- Beam Computed Tomography vs. Photoacoustic Tomography (μ -CT vs. CBCT vs. PAT)	38
3.1.1	Micro-Computed Tomography vs. Photoacoustic Tomography (μ -CT vs. PAT).....	39
3.1.2	Micro-Computed Tomography vs. Cone-Beam Computed Tomography (μ -CT vs. CBCT)	40
3.1.3	Photoacoustic Tomography vs. Cone-Beam Computed Tomography (PAT vs. CBCT)	41

3.2	Surface and Volume Deviations: Micro-Computed Tomography (μ -CT) vs. Cone-Beam Computed Tomography (CBCT) vs. Photoacoustic Tomography (PAT)	42
3.2.1	Photoacoustic Tomography vs. Micro-Computed Tomography (PAT vs. μ -CT)	46
3.2.2	Cone-Beam Computed Tomography vs. Micro-Computed Tomography (CBCT vs. μ -CT)	46
3.2.3	Photoacoustic Tomography vs. Cone-Beam Computed Tomography (PAT vs. CBCT)	47
4	Discussion	48
4.1	Accuracy of PAT	49
4.2	PAT for Daily Clinical Practice in Dentistry	50
4.3	PAT Compared With Other Non-Ionizing Imaging Techniques	51
4.3.1	Ultrasound	51
4.3.2	MRI	51
4.3.3	OCT	52
4.4	PAT for Daily Clinical Practice in Other Medical Applications	52
4.4.1	Brain Imaging	52
4.4.2	Thyroid Imaging	52
4.4.3	Breast Imaging	53
4.4.4	Dermatological Imaging	53
4.5	Outlook for PAT in Daily Clinical Practice	54
4.6	Study Limitations	54
5	Summary	55
6	Appendix	57
6.1	Materials	57
6.1.1	Equipment	57

6.1.2	Consumables.....	57
6.1.3	Solutions.....	58
6.1.4	Software	59
6.2	Reference List.....	60
6.3	Scientific Publications of the Pilot Study	70
6.3.1	Poster Presentation in Rostock (Germany) 2019.....	70
6.3.2	Oral Presentation in Vancouver (Canada) 2019	71
6.4	Ethics Committee Vote.....	72
6.5	Informed Consent Form and Patient Information for Extracted Teeth	73
6.6	Acknowledgments	1
6.7	Curriculum Vitae.....	3

List of Abbreviations

μ -CT	Micro-Computed Tomography
μ Sv	Microsievert
ALARA	As Low As Reasonably Achievable
CBCT	Cone-Beam Computed Tomography
Fig.	Figure
HU	Hounsfield Unit
IQR	Interquartile Range
m/s	Meter/Second
MHz	Megahertz
MRayl	MKS Rayl
MRI	Magnetic Resonance Imaging
MSOT	Multispectral Optoacoustic Tomography
mSv	Millisievert
PAT	Photoacoustic Tomography
PETG	Polyethylene Terephthalate
Q1	First Quartile
Q3	Third Quartile
RSA	Root Surface Area
RSD	Root Surface Deviation
SD	Standard Deviation
TIFF	Tagged Image File Format
US	Ultrasound
VD	Volume Deviation
Vol%	Percent by Volume
vs.	Versus

1 Introduction

Conventional imaging modalities in general dental practice include numerous radiographic techniques for the diagnosis of several pathologies affecting the teeth and bones of the maxillofacial region [1]. However, conventional dental imaging techniques (single-tooth radiographs or panoramic imaging [2]) have two major disadvantages: interposition of anatomical parts and poor detail on images (due to under/overexposure [3]). To overcome these limitations, the three-dimensional reconstruction of teeth in dentistry has gained fundamental importance in the last two decades [4]. Nowadays, several imaging devices are available in dentistry to create three-dimensional reconstructions [5]. However, the imaging techniques commonly used in dental practice to create three-dimensional images are still based on x-rays. Although these techniques can overcome the interposition of anatomical parts and poor detail on images, ionizing radiation still poses a severe problem due to its ability to cause temporary and permanent tissue damage [6]–[11].

The frequency of radiological examinations in dentistry compared with in other medical disciplines in Germany is shown in Fig. 1. This figure illustrates that, at 42%, dentistry accounts for the biggest share of x-ray images taken in everyday clinical practice [12].

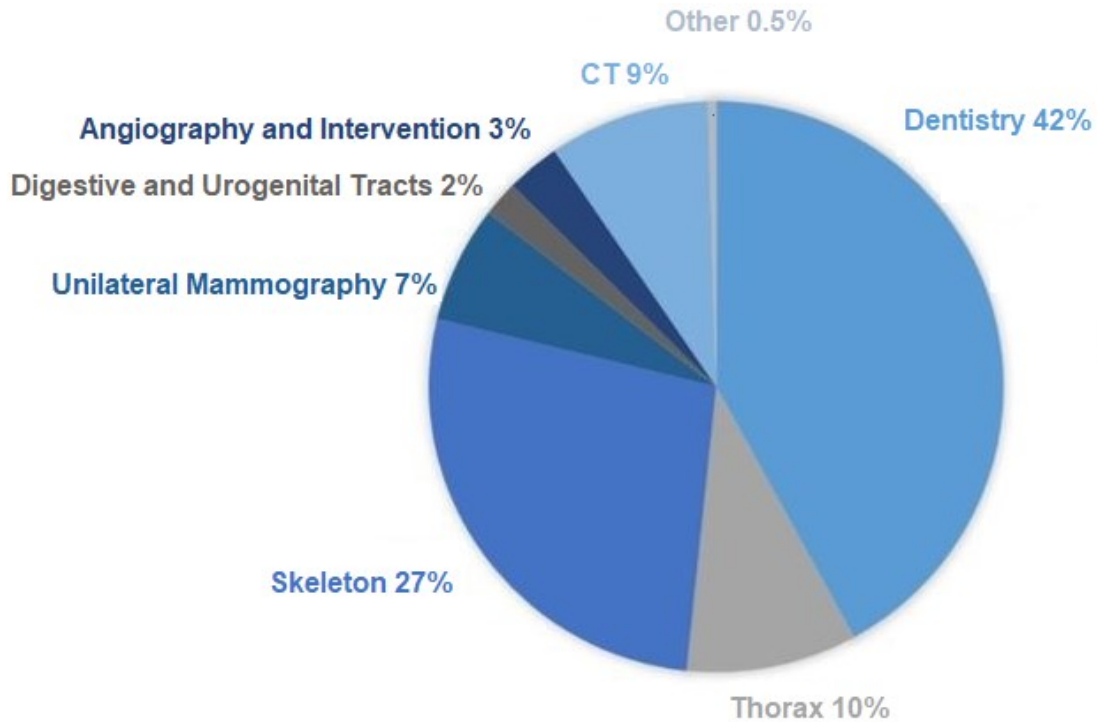


Fig. 1. Percentage share of different radiological examinations with regard to overall frequency. In Germany, x-rays are most frequently used in dentistry. With permission from BfS (Bundesamt für Strahlenschutz, 2020) [13].

Although x-rays have many useful applications, their potential risks must be taken into consideration. X-rays can cause the ionization of water molecules, creating hydroxyl radicals that can interact with deoxyribonucleic acid (DNA), causing strand breaks or base damage. DNA can also be ionized directly. This can result in point mutations, chromosome translocations, and gene fusion, which are linked to cancer induction [6], [7].

In Europe, the “ALARA principle” (“As Low As Reasonably Achievable”) has general validity in clinical practice. This means that the least possible radiation exposure must be applied to gain the maximum imaging resolution [14].

In Germany, the Federal Law Gazette stipulates that every time an x-ray is taken, the benefit must outweigh the risk and the procedure must be justified and documented [15].

Based on these regulations, the use of diagnostic x-rays in children and pregnant or lactating women is strictly limited [16].

To avoid ionizing radiation exposure during medical imaging, several non-invasive modalities for creating three-dimensional images have been introduced:

- magnetic resonance imaging (MRI) based on magnetism [17],
- ultrasound (US) based on sound [18], and
- optical coherence tomography (OCT) based on light [19].

These techniques have the advantage of utilizing non-ionizing radiation. In addition, although these methods are better suited to visualizing soft tissue, they are increasingly being used for hard tissue as well [20]–[22].

Photoacoustic tomography (PAT) is a very innovative and promising imaging technique. It is based on sound and non-ionizing light in the near-infrared range. This combination of light and sound ensures a higher scalability of spatial resolution and depth penetration, due to the fact that acoustic waves are less scattered in tissue than photons are. This emerging technique has been tested on a variety of different biological tissues in several diseases (e.g. breast cancer, atherosclerosis). Most of these applications exploit endogenous chromophores such as hemoglobin, melanin, and lipids, which possess specific absorption spectra. The identification of additional absorption spectra would enable the clinical applications of PAT to be extended [23].

Regarding the current state of the art, PAT can be used to examine soft tissue in the human body by applying wavelengths of between 650 and 900 nm [24]. To apply PAT in dentistry, it would be beneficial if this technique could also depict hard tissues, such as dentin. To be able to do so, however, it is essential to know details about the individual absorption spectrum of the tissue in question, which depends on its composition. The following sections therefore give an overview of the structure of human teeth, with a focus on the optical properties of the different tissues of the teeth.

1.1 Structure of Teeth

Each human tooth can be divided into four parts: enamel, dentin, cementum, and pulp (Fig. 2).

The main mass of the tooth consists of dentin [25], which is covered by enamel in the upper area [26] and by a thin layer of cementum in the cervical area [27]. The pulp is located in the center of the tooth [28].

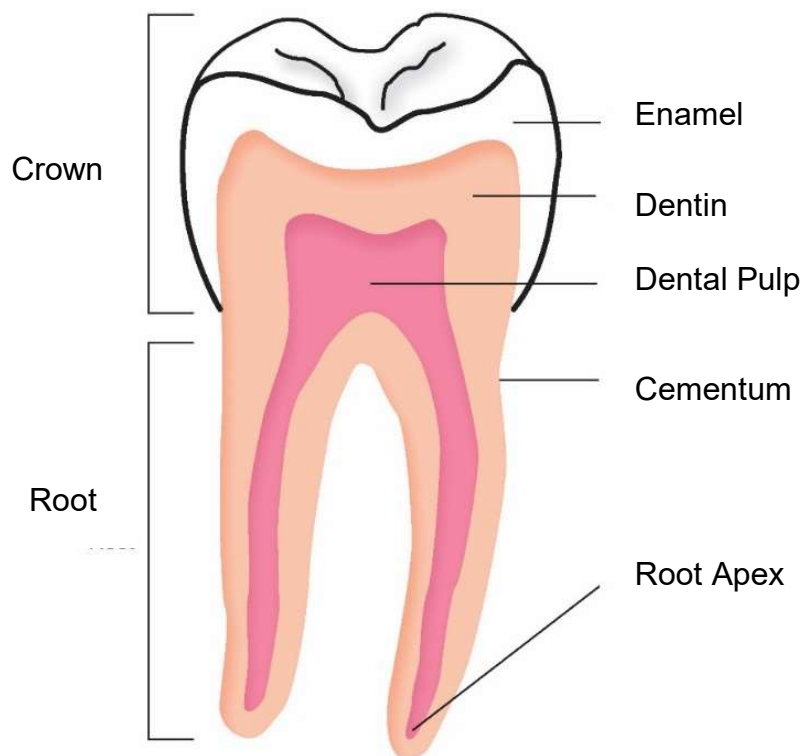


Fig. 2. Schematic drawing of a tooth. The tooth can be divided into enamel, dentin, cementum, and pulp.

1.1.1 Enamel

1.1.1.1 Chemical Structure

During tooth development, preameloblasts are converted into ameloblasts and start to deposit enamel matrix [29]. This enamel matrix starts to calcify in rhythmic phases, forming calcium phosphate crystals. The gaps between the individual crystals remain as micro-porosities in the enamel matrix. After the tooth erupts, these little porosities are largely balanced by the uptake of calcium and phosphate from the saliva accompanied by the simultaneous loss of water [30]. The mineral content by volume of initially deposited enamel is 25-30% [31]. During enamel maturation, the mineral content increases to 86%, thus representing the biggest share of the enamel, followed by the water content (12%) and the organic matrix (2%) [32].

The water within the enamel matrix is either linked to crystallites or loosely embedded in the organic matrix. The small amount of organic matrix is made up of soluble and insoluble proteins that contain amino acids such as glutamine, leucine, glycine, and serine. The inorganic content is dominated by phosphorus and calcium, which is formed in the shape of a hydroxyapatite with the chemical formula $\text{Ca}_{10}(\text{PO}_4)_6(\text{OH}_2)$ [32].

1.1.1.2 Histological Structure

Enamel is the hardest and stiffest tissue of the human body. These outstanding mechanical properties are the result of the unique hierarchical microstructure of the enamel, enabling the tooth to withstand everyday mechanical stress [29].

To understand the optical properties of enamel, it is necessary to have a closer look at its histological structure. According to He [29], the rod unit is “...*the most important level in understanding the microstructure and function of enamel.*”

The mineral content consists of calcium phosphate crystallites. These crystallites form hexagonal sticks with dimensions of $25 \times 40 \times 160$ nm, thus making them larger than the crystallite prisms of bone, dentin, or cementum [34].

The prisms (rods) are oriented nearly perpendicular to the surface of the tooth and are connected to each other, influencing the optical properties of the enamel (see 1.1.4) [35].

With respect to the optical axis of the enamel, the findings in the literature are inconsistent. In 1982 Schroeder claimed that one optical axis exists, which is parallel to the long axis of the prisms [34], whereas Duplain (1987) claimed that the optical axis (c-axis) of the hydroxyapatite crystals can be divided into two subgroups, “...one with their c-axis parallel to the long axis of the tooth and the other with their c-axis perpendicular to the long axis of the tooth as well as the surface” [35].

However, by 1965 Meckel, Griebstein, and Neal had already discovered that enamel prisms have a “keyhole shape” in cross-section [36]. Today a distinction is made among “keyhole,” “horseshoe,” and “cylindrical” prisms [37].

1.1.2 Dentin

1.1.2.1 Chemical Structure

The organic matrix of dentin accounts for 30% of its structure. Dentin has a relatively low mineral content (45%) that mostly consists of calcium and phosphorus. Its water content is approximately 25% [38].

1.1.2.2 Histological Structure

Starting from the outermost layer, dentin can be divided into mantle dentin, circumpulpal dentin, and predentin [39].

Mantle dentin has a thickness of approximately 80–100 μm and is located immediately below the enamel–dentin border. Circumpulpal dentin is located

below the mantle dentin and comprises the largest portion of the dentin. Predentin is directly bonded to the circumpulpal dentin [36]. In mature dentin, the Tomes' fibers are surrounded by peritubular dentin. The matrix between the peritubular dentin is called intertubular dentin [38].

Moving from the periphery of the dentin toward the pulp chamber, the layer thickness of dentin changes, and the number and size of the dentin tubules also change. Close to the pulp, the density of tubules is high and lies between 30 000 and 50 000/mm². Approaching the enamel–dentin border, the density of tubules decreases, ranging between 10 000 and 25 000/mm² [36], [40]. These tubules have an important impact on the optical properties of dentin (see 1.1.4).

In their study, Zolotarev and Grisimov demonstrated that horizontal sections of molars exhibit the optical properties of an object composed of numerous uniaxial crystals with different optical axes. In addition, it was shown that the dentin in the center parts of the section behaves like an uniaxial crystal [41].

With respect to absorption and scattering coefficients, Zijp showed that absorption and scattering have their maximum coefficient at ≈ 400 nm. However, both absorption and scattering coefficients depend on the position of the dentin within the tooth [42].

1.1.3 Pulp

The pulp is located in the center of the tooth and consists of a neurovascular bundle [28]. Several types of cells can be found in the pulp, including fibroblasts, odontoblasts, histiocytes, and macrophages. These cells are responsible for the vitality and reactivity of the tooth. However, the pulp also contains undifferentiated cells, whose natural function lies in the production of odontoblasts. Thus, these cells preserve the ability of the pulp to self-renew [43].

Whereas the configuration of the crown of certain tooth types shows little variation, the configuration of the root shows numerous variations [36]. The root canal system and apical region, in particular, can vary greatly between individuals

[43]. For this reason, x-ray based imaging techniques are used before endodontic treatment, for example.

The nutritive function of the tooth is ensured by a blood vessel system and innervation. However, blood circulation in the pulp adapts very poorly to high temperatures above 40°C, resulting in damage to the cells or even cell death [43]. This is important to keep in mind, because PAT causes a temperature increase in the tissue being examined [44].

1.1.4 Optical Properties of Dentin and Enamel

Because light plays a key role in photoacoustic tomography, basic knowledge of the light-conducting properties of materials is required.

1.1.4.1 Refractive Index

The refractive index is used to characterize the optical properties of materials. The refractive index “ n ” is dimensionless and describes the ratio of lightspeed in a vacuum in relation to the lightspeed in a material/tissue. Consequently, the refractive index describes the degree to which a ray of light bends when passing from one medium into another. To calculate the refractive index, the angle of incidence of a ray in a vacuum (i) is set in relation to the angle of refraction (r) [45].

To enable comparisons between the optical properties of different media, the refractive index in a vacuum is set to $n=1$, whereas water has a refractive index of $n=1.33$ [45]–[47].

The refractive index of the tooth changes within its different layers (e.g. enamel, dentin, pulp) and decreases from the enamel to the pulp, proportional to the density of the tissue. In addition to density, the orientation of the crystalline structures affects the optical properties of the tooth (see 1.1.1. and 1.1.2) [48].

1.1.4.1.1 Refractive Index of Enamel

Spitzer and Ten Bosch [49] determined the transmission and reflectance of thin slabs of bovine and human tooth enamel in 1975. Regarding the refractive index of the different slabs, no significant differences could be found. They verified the refractive index of both types of enamel to be approximately 1.625 in the visible spectrum of light, whereas the refractive index at a wavelength of 220 nm was approximately 1.725.

The light absorption spectrum of human enamel is also important. The maximum absorption spectrum appears to have a range between 235 nm and 270 nm [49].

1.1.4.1.2 Refractive Index of Dentin

Compared with the refractive index of enamel, the refractive index of dentin is closer to 1. However, the refractive indices of dentin differ between its various layers, according to their composition (see 1.1.2). Peritubular dentin has the highest value (1.59). This can be explained by the high mineral content of peritubular dentin. Tubules, in contrast, do not contain any minerals; therefore, their refractive index (1.33) is lower than that of peritubular dentin. Averaging the refractive indices for all dentin layers results in a refractive index of 1.49 [26].

1.1.5 Acoustic Properties of Dentin and Enamel

Acoustics play an important role in PAT. Consequently, a basic understanding of the acoustic properties of dental tissue is needed.

The photoacoustic effect is an energy-transforming process whereby intensity-modulated optical radiation is transformed into acoustic waves [50].

Barber, Lees, and Lobene [51] were the first to assess the acoustic properties of human teeth in 1969. In their study, an ultrasonic pulse-echo system was successfully applied to detect the dentin–enamel junction and dentin–pulp interface. This was achieved by measuring the velocity of sound for longitudinal

waves in intact human teeth. A longitudinal sound velocity of 6250 m/s in enamel and 3800 m/s in dentin was found for human incisors.

In 2002, Ghorayeb [21] determined the acoustic properties of teeth by using a non-invasive ultrasound system. In that study, teeth were ground to an almost flat surface, fixed in a plexiglass holder, and immersed in water in order to analyze their acoustic properties.

The longitudinal sound velocity was found to be 6250 m/s in enamel, 3800 m/s in dentin, and 1570 m/s in the pulp, confirming the values for enamel and dentin presented by Barber, Lees, and Lobene [51] in 1969.

Interestingly, acoustic impedance decreased, in accordance with longitudinal sound velocity, from the enamel (18.75 MRayls) to the pulp (1.57 MRayls) [21].

1.2 State-of-the-Art Imaging Techniques

Most imaging techniques used in daily clinical dental practice are based on x-rays. Imaging approaches typically include simple x-ray devices that are used to create two-dimensional radiographs, but also sophisticated imaging techniques, such as cone-beam computed tomography (CBCT), which is used to create complex three-dimensional images [1].

To provide an overview of the complex issue of ionizing imaging techniques, the following sections of the current chapter explain the basics of CBCT and micro-computed tomography (μ -CT). The next chapter, "Materials and Methods," provides a more detailed description of the CBCT and μ -CT set-ups used in this thesis.

At the end of the current chapter, descriptions are given of the most common non-ionizing imaging techniques, such as magnetic resonance imaging (MRI), ultrasound (US), and optical coherence tomography (OCT).

1.2.1 Ionizing Imaging Techniques

The history of ionizing imaging techniques started on November 8, 1895 in Wuerzburg, Germany. On this day, Wilhelm Conrad Roentgen discovered the illumination of a barium–platinum fluorescence screen even though it was covered by a lightproof box. He investigated the radiation and, after weeks of examination, in January 1896 published the physical characteristics of the radiation under the name “x-rays,” thereby establishing the basis for new imaging techniques. A few months after this discovery, the first ionizing imaging devices were already in use [52].

X-rays are electromagnetic waves with wavelengths ranging from 10^{-8} m to 10^{-12} m [53]. To generate x-rays, a tube is used to speed up and slow down electrons. This x-ray tube consists of a cathode and an anode that face each other. Both are incorporated in a vacuum glass cylinder. A high voltage is generated between the cathode and the anode, speeding up the electrons that are issued from the cathode. The moment the accelerated electrons collide with the anode, they instantly slow down. This sudden change of speed leads to the release of thermal energy and x-rays. The x-rays are directed onto the research object, resulting in an interaction between the research object and x-rays. The energy of the x-rays is transmitted to the research object and thereby weakened. The modified x-rays then hit a conventional x-ray film or detector [54], [55].

1.2.1.1 Computed Tomography (CT)

CT was established in medicine in the 1950s, enabling the creation of three-dimensional images [56].

To produce tomographic images, a computer-processed combination of multiple radiographs are taken from different angles. The general basis for the reconstruction of the images is the “Radon transformation,” which was published in 1917 by Johan Radon [56].

The spatial resolution of a three-dimensional image largely depends on the positioning of the patient [57]. If the patient does not move during image

acquisition, spatial resolutions of up to 0.3 mm can be achieved. However, the higher the spatial resolution, the greater the radiation exposure for the patient. Therefore, a step size (distance between one picture to the next) between 1 and 5 mm is usually chosen [58]. On average, the patient is exposed to a radiation load of 788 μSv [4]. By comparison, the natural radiation exposure per year is approximately 2.1 mSv [59].

To reach a higher spatial resolution, $\mu\text{-CT}$ can be used. $\mu\text{-CT}$ -images can reach a spatial resolution of 1–100 μm . This makes $\mu\text{-CT}$ especially suitable for examinations in the biomedical sciences sector, but also in basic medical and dental research [60].

1.2.1.2 Cone-Beam Computed Tomography (CBCT)

CBCT entered the European dental market in 1996 [61]. Compared with CT, CBCT has a big advantage in terms of radiation exposure, which ranges from 100 to 150 μSV . Thus, the potential risk of tissue damage in patients is significantly reduced compared with CT. For this reason, CBCT is used in many dental sectors and has almost replaced CT in dentistry [62].

This imaging technique creates pictures with a spatial resolution of up to 75 μm . Similar to CT, the spatial resolution of CBCT can be adversely affected by any type of metal or patient movement during image acquisition [63].

1.2.2 Non-Ionizing Imaging Techniques

Ultrasound (US), magnetic resonance imaging (MRI), optical coherence tomography (OCT), and photoacoustic tomography (PAT) are non-invasive imaging modalities that do not utilize ionizing radiation. These modalities are described in the following sections, in order of their chronological discovery [17], [18], [23], [64].

1.2.2.1 Ultrasound (US)

Ultrasound is a low-cost and non-invasive imaging method that is based on sound. The history of US starts in 1875. At this time, Robert Hooke foresaw the use of sound for diagnostic purposes when he wrote (Tyndall, 1875): “... *It may be possible to discover the motions of the internal parts of bodies, weather animal, vegetable, or mineral, by the sound they make ...*” [65].

Although US was used in the early 1900s in technical settings, the first medical devices were developed in the late 1920s. As a result, US physiotherapy became popular in the 1930s. In the following years, US applications were developed further, and nowadays this technique is successfully used in several medical disciplines [66].

To create three-dimensional images, most US devices generate ultrasound frequencies between 1 and 15 MHz. The transmitted pulse infuses the region of interest until it encounters an “acoustic” interface. Right at that moment, one part of the pulse is absorbed while the other part is reflected back. Once the reflected pulse hits a transducer, the magnitude of voltage and time needed for the echo to come back is measured. Based on these pieces of information, the location of the acoustic interface can be reconstructed. Furthermore, the speed of the sound provides information about the density of the tissue. By matching the various voltage magnitudes to a certain brightness level, an image can be reconstructed [18].

The spatial resolution of US images depends on the wavelength of the sound that was used to generate the image. For example, a resolution of 0.3 mm can be achieved if the US beam has a wavelength of 5 MHz [67].

The penetration depth of US in general is affected by receiver gain; output power; frequency and efficiency of the transducer; and signal processing within the US machine [67]. The penetration of US devices is especially limited by the available frequencies [68], which range from 1 to 15 MHz [18]. Further limitations are imposed by the acoustic noise of the reflected pulse, which is often weaker than the sound within the image and therefore cannot be detected (e.g. in blood vessels).

However, the quality of the image is not only affected by adjustable factors, but also by factors that cannot be influenced, such as artifacts. Common artifacts are “acoustic shadows” or “refraction artifacts.” An “acoustic shadow” occurs when the sound energy transmitted beyond the region of interest is too weak to generate a detectable echo signal. “Refraction artifacts” occur when the transmitted sound or reflected echo is bent at a boundary between tissues [18].

1.2.2.2 Magnetic Resonance Imaging (MRI)

MRI is a non-invasive imaging technique that uses non-ionizing radiation. Like CT and CBCT, MRI can generate three-dimensional images.

To create a three-dimensional MRI image, a strong external magnetic field is generated to influence the nuclear spin (of hydrogen), resulting in a modified rotation of the nuclei at a certain frequency, the so-called “Larmor frequency.” Once all nuclei are at the Larmor frequency, a second magnetic field perpendicular to the original magnetic field is turned on. This magnetic field has the same frequency as the Larmor frequency of the nuclei. The nuclei therefore start to tilt in another direction. Once the second magnetic field is turned off again, the nuclei start to tilt back in their original direction (nuclear magnetic resonance). Depending on the tissue type, the nuclei need different amounts of time to tilt back and thereby generate a signal. The intensity of the signals is recorded and afterwards reconstructed by a computer. The result is a grayscale three-dimensional image.

Both hard and soft tissues can be imaged using MRI, which is an important advantage of this technique [17]. For this reason, MRI is often used in dentistry to examine changes to the cartilage structure of the temporomandibular joint or to find the cause of limitations in jaw opening. [4], [14], [69]–[71]. However, MRI also has other applications in dentistry; for example, it can be used to image human teeth and maxillofacial bones [72].

MRI images can also be affected by artifacts. Patient movement [22], artifacts caused by dental filling materials [72], problems with hardware (e.g.

inhomogeneous magnetic fields), and inaccurate data processing (e.g. objects that are smaller than the size of voxels) can reduce the quality of images [73].

1.2.2.3 Optical Coherence Tomography (OCT)

OCT is a non-invasive medical imaging technique that uses light [19], [74]. OCT was developed in 1991, and it took five years until the first commercial OCT device was launched [19], [64].

To generate an OCT image, a low-coherence light beam (whose wavelength is close to the wavelength of infrared) is split into two equal rays. One ray is focused on the tissue of interest, and the other is pointed at a reference mirror. The two backscattered rays of light are recombined, resulting in a phenomenon called “interference.” The interference can be measured by a photodetector receiver, and an image can be reconstructed based on these data. [75].

By applying this imaging technique in vitro, it is possible to generate two-dimensional images with a spatial resolution in the range of 1 μm to 15 μm [20]. The major shortcoming of OCT is its limited penetration depth, which lags behind that of CT, MRI, and US. If a suitable wavelength is chosen, a penetration depth of 1–2 mm can be reached [76]. A wavelength of 830 nm can acquire images of the human skin with a penetration depth of 0.5–1.5 mm [77].

However, OCT is not free of artifacts: curved and discontinuous surfaces can result in distorted, poor-quality images [78].

1.2.2.4 Photoacoustic Tomography (PAT)

PAT or optoacoustic tomography is one of the latest imaging techniques. It combines the advantages of US and OCT by emitting light to receive sound waves. This effect is called the photoacoustic effect, and was discovered in 1880 by Alexander Graham Bell [79]. He noted that chopped sunlight creates a sound once it hits an optical absorbing material. Approximately 100 years after his discovery, it was possible to examine gases and solids by using this technique.

In 1994, the first method for the examination of biological tissues using PAT was presented [80].

Nowadays, it is possible to create three-dimensional images in real time using modern photoacoustic tomographs. To create photoacoustic images, non-ionizing, red-shifted, nanosecond-long pulsed laser light is pointed at the tissue of interest [23] (Fig. 3).

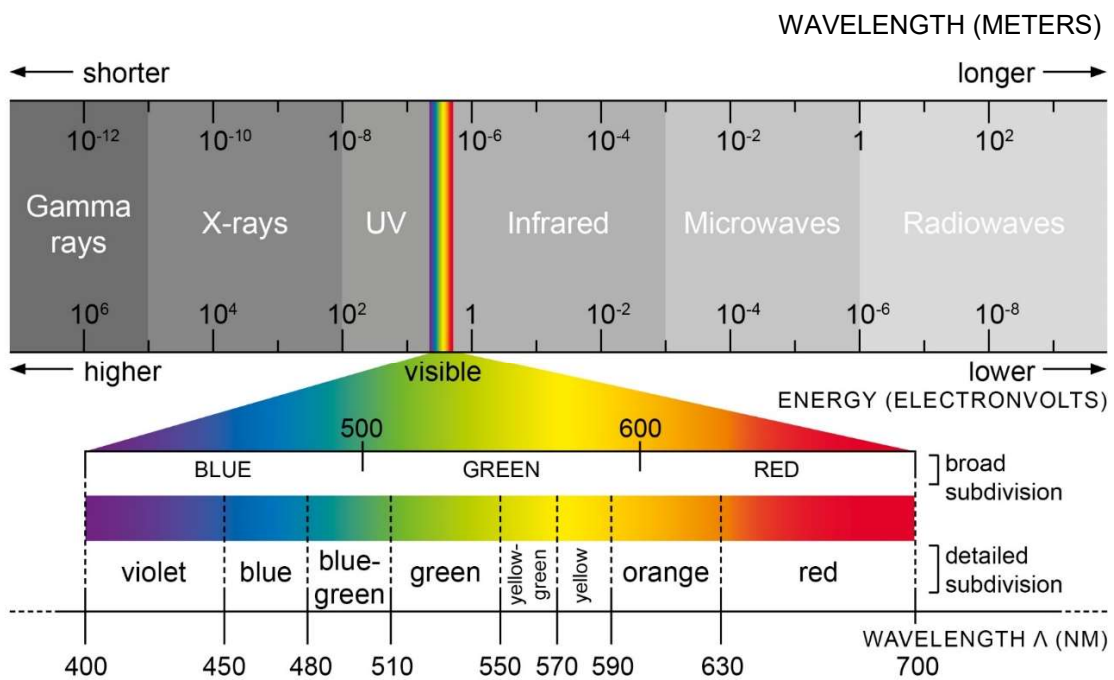


Fig. 3. Electromagnetic spectrum. The electromagnetic spectrum is the total of all electromagnetic waves with frequencies from below one hertz to above 10^{25} hertz. The light spectrum is the part of the electromagnetic spectrum that is visible to humans. With permission from ACS Publications – Verhoeven et al. (2017), Brose et al. (2011) [81], [82].

The wavelength of visible red light ranges from 650 nm [83] to 780 nm [82]. Infrared light, which is invisible to humans, can be divided into IR-A light (780–1400 nm), IR-B light (1400–3000 nm), and IR-C light (3000 nm–1 mm). [82]. Most photoacoustic devices use wavelengths of 660–1300 nm for in-vitro imaging and 650–980 nm for in-vivo imaging [84] (Fig. 4).

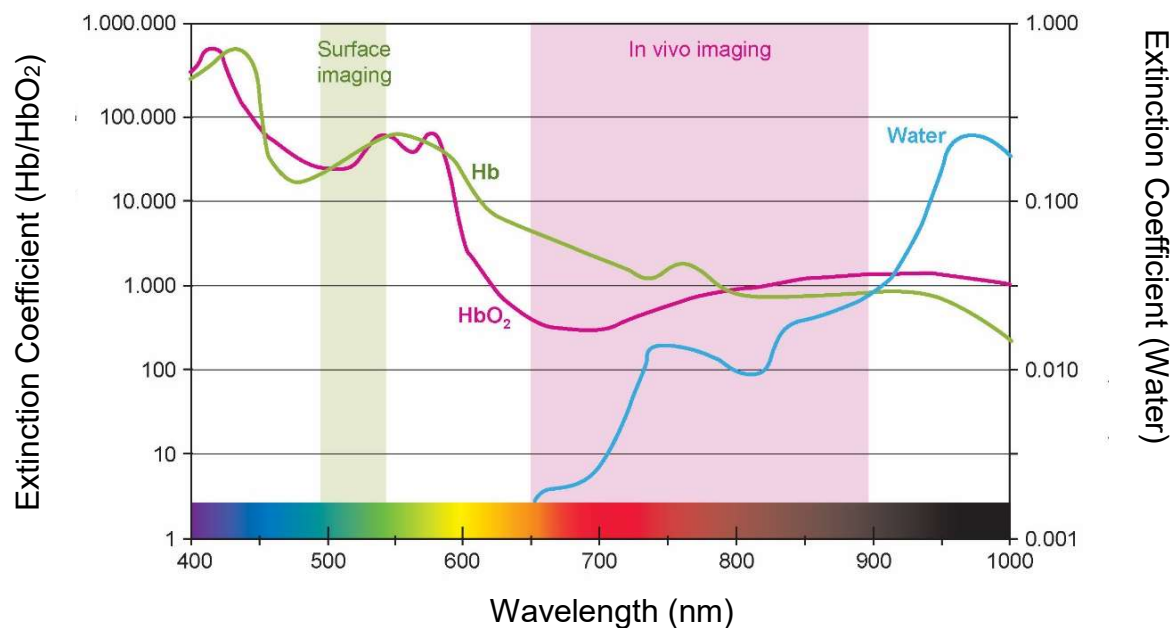


Fig. 4. Extinction coefficient values of water and oxy- and deoxy-hemoglobin. The optical window used for in-vivo imaging ranges from 650 nm to 900 nm. Here, maximum tissue penetration can be reached due to minimal absorbance and autofluorescence of chromophores. Ultraviolet light can cause direct tissue damage. Blue-green light has poor tissue penetration and therefore can only be used for surface imaging or small-animal imaging. With permission from ACS Publications – Kobayashi et al. (2010) [24].

Light with a wavelength shorter than 650 nm is not suitable for imaging for several reasons. Ultraviolet light can cause direct tissue damage. Blue-green light has poor tissue penetration and can therefore only be used for surface imaging or small-animal imaging. Use of yellow or red light with a wavelength of ≈ 600 nm leads to increased absorption of a large proportion of naturally occurring endogenous fluorophores.

Thus, wavelengths in the near-infrared range combine several positive properties: good tissue penetration, low autofluorescence, and the ability to generate the heat necessary to create pressure waves without causing damage to the tissue [24].

Once the tissue of interest has been penetrated by a pulsed, nanosecond-long, red-shifted laser beam, the light is absorbed by endogenous chromophores, such as hemoglobin, melanin, water, and lipids (Fig. 5). The absorbed light is converted into thermal energy, resulting in local heating of the tissue. The localized heating results in a thermoelastic expansion, which causes the emission of pressure waves (ultrasound). These pressure waves can be detected by an array of multiple broadband ultrasonic transducers and are converted into high-resolution images [23], [85].

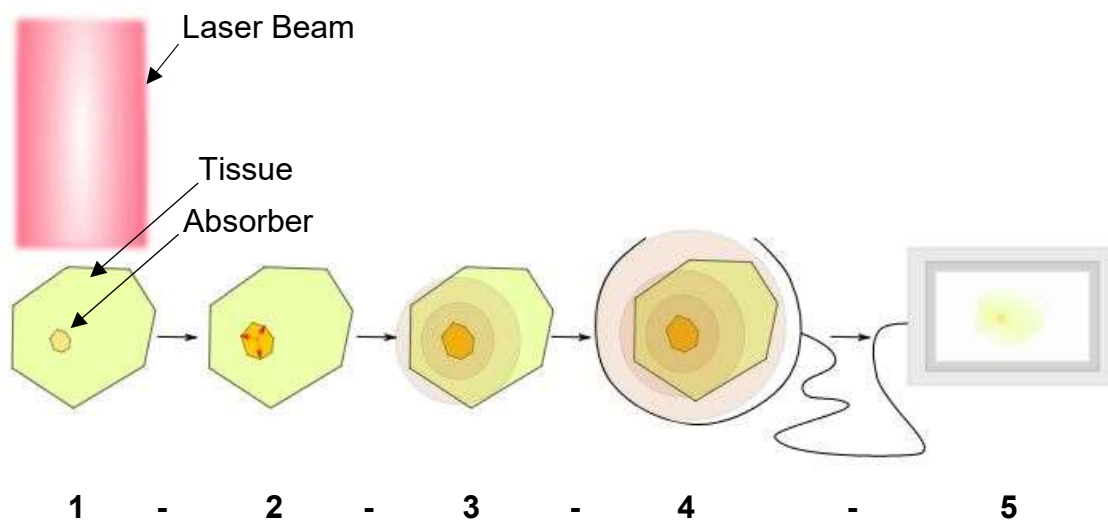


Fig. 5. Principle of photoacoustic tomography. **(1)** Red-shifted light hits the tissue of interest and is absorbed by endogenous chromophores such as hemoglobin, melanin, water, and lipids. **(2)** The absorbed light is converted into thermal energy, resulting in local heating. The localized heating leads to thermoelastic expansion, which causes **(3)** the emission of pressure waves (ultrasound). **(4)** These pressure waves create a sound that can be detected by an array of multiple broadband ultrasonic transducers **(5)**, and the sound is converted into high-resolution images [23], [85].

Each chromophore has a different absorption spectrum, resulting in different light-absorption characteristics. Unfortunately, some tissue components share a very similar absorption spectrum, which makes it difficult to distinguish these tissues using PAT. In these cases, exogenous imaging agents can enhance the contrast, as shown in both in-vitro and in-vivo studies [23], [86].

Other relevant issues regarding PAT are the penetration depth of the light and the spatial resolution, which are both affected by similar factors: the acoustic center frequency, the bandwidth, and the aperture of the ultrasound detection system. The scattering of light is also a problem, because it prevents the light pulse from penetrating deep into the tissue [87]. Finally, penetration depth depends on the density of the tissue of interest. Penetration is much greater in soft tissue than in hard tissue [23]. Manohar et al., for example, achieved a maximum penetration depth of 60 mm in the female breast using a wavelength of 1064 nm [88].

1.3 Aim of the Present Study: Hypothesis

Dental imaging is a crucial tool for diagnosing several pathologies affecting the teeth and bones of the maxillofacial region. In the context of new treatment options, such as guided implant surgery and individual dental implants, three-dimensional imaging has gained fundamental importance in dentistry and achieved remarkable therapeutic successes. However, the imaging techniques commonly used in dental practice to create three-dimensional images are still based on x-rays. Although these techniques can overcome the interposition of anatomical parts and poor detail on images, ionizing radiation still poses a severe problem due to its ability to cause temporary and permanent tissue damage. As mentioned, PAT is an innovative and promising alternative imaging technique that is based on red-shifted light and sound [23].

The principal objective of this thesis was to assess the accuracy of PAT based on volume and surface deviations of mandibular teeth. This included the comparison of three-dimensional models of the teeth based on PAT with corresponding three-dimensional models based on μ -CT and CBCT.

In addition to assessing volume and surface deviations, this thesis sought to determine the best wavelength to acquire photoacoustic images of the teeth.

The study had two specific objectives:

1. to determine the best wavelength to acquire photoacoustic images of the teeth
2. to create three-dimensional models based on PAT and CBCT, and to compare them with models based on the reference imaging method μ -CT with respect to volume and surface deviations.

The null hypotheses were that

1. the total volume of human mandibular incisors assessed in vitro by using PAT and CBCT would not significantly differ from the total volume assessed by using μ -CT, and
2. surface deviations between μ -CT–CBCT and μ -CT–PAT would not differ significantly.

2 Materials and Methods

2.1 Preliminary Experiments

2.1.1 Teeth

Five extracted human, single-rooted teeth of the lower and upper jaw, comprising teeth #23, 32, 12, 44, and 42 (FDI World Dental Federation notation), were collected and cleaned with the aid of an ultrasonic scaler (SONICflex LUX 2000L, Germany). According to its shape, each tooth had a different size. After extraction, the teeth were stored for two days in a 1% chloramine-T solution at 5°C. The teeth were also anonymized, to prevent any individual tooth from being attributed to a specific patient.

This study was conducted in compliance with the Declaration of Helsinki, and the use of extracted human teeth was approved by the Medical Ethics Committee of the University of Wuerzburg (application number 15/15). All patients provided written informed consent. An example of the informed consent form can be found in the annex.

In the pilot study, μ -CT and PAT were used. CBCT was used in addition in the main study only.

2.1.2 Experimental Setup: Micro-Computed Tomography (μ -CT)

To acquire μ -CT images, teeth were scanned using a μ -CT device (MetRIC - Micro and Region of Interest CT, Fraunhofer IIS; Wuerzburg, Germany). The MetRIC can reach a spatial resolution of up to 2 μ m and a magnification of up to 630 \times . The setup for μ -CT acquisition is shown in Fig. 6 [89].

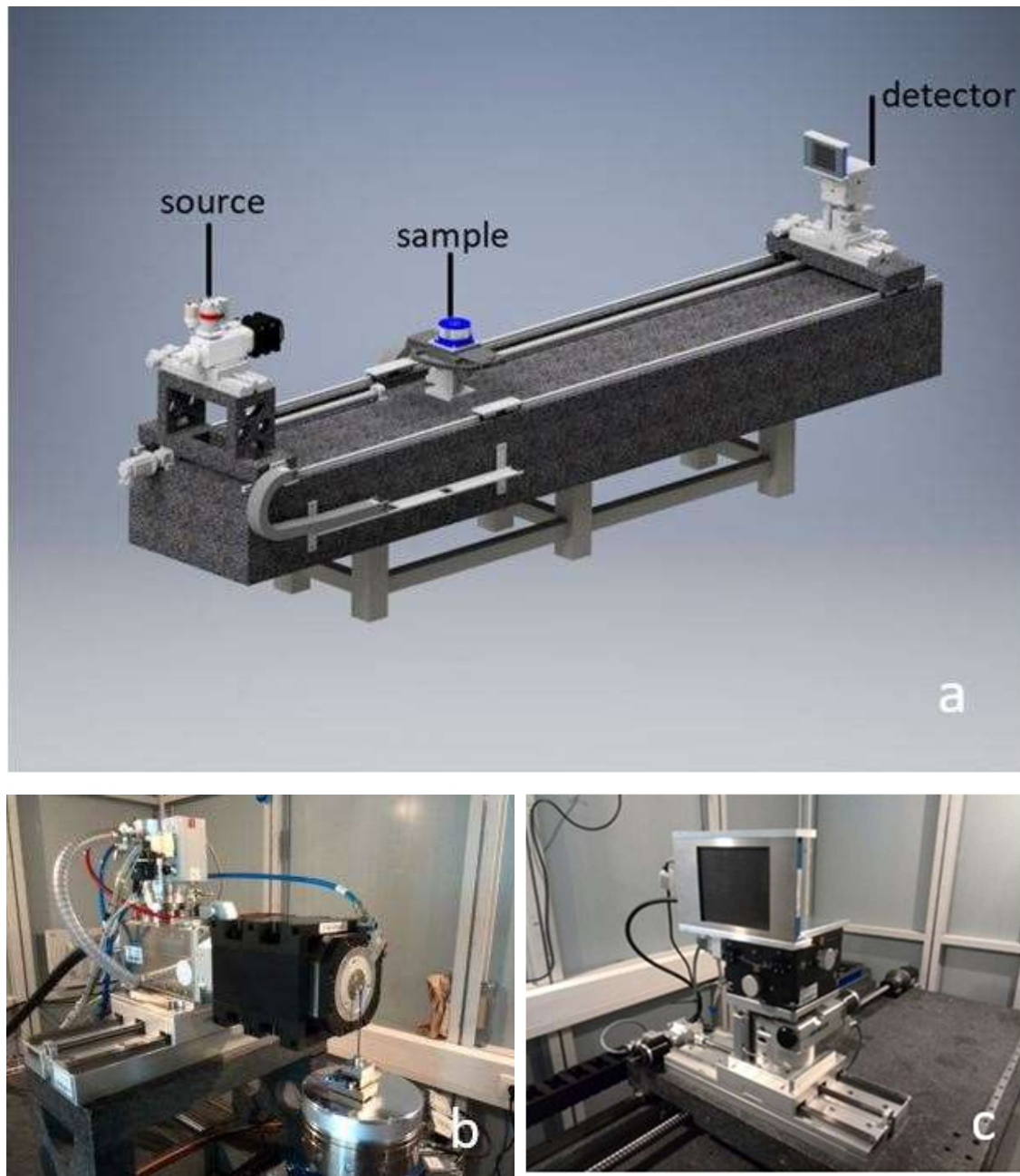


Fig. 6. MetRIC (Micro and Region of Interest CT). To create μ -CT images, teeth were scanned with the MetRIC. (a) Schematic image of the MetRIC. (b) Source of MetRIC. (c) Detector of MetRIC. With permission from the Institute for X-ray Microscopy, Fraunhofer IIS; Wuerzburg, Germany.

To attach the teeth to the sample holder, each tooth was held in place with Oasis foam (Gravidus GmbH; Bremen, Germany) in a screw-capped centrifuge tube that was filled with 1% chloramine-T solution (Fig. 7). The μ -CT acquisition itself resulted in a stack of two-dimensional images of each tooth, which was saved in tagged image file format (TIFF).

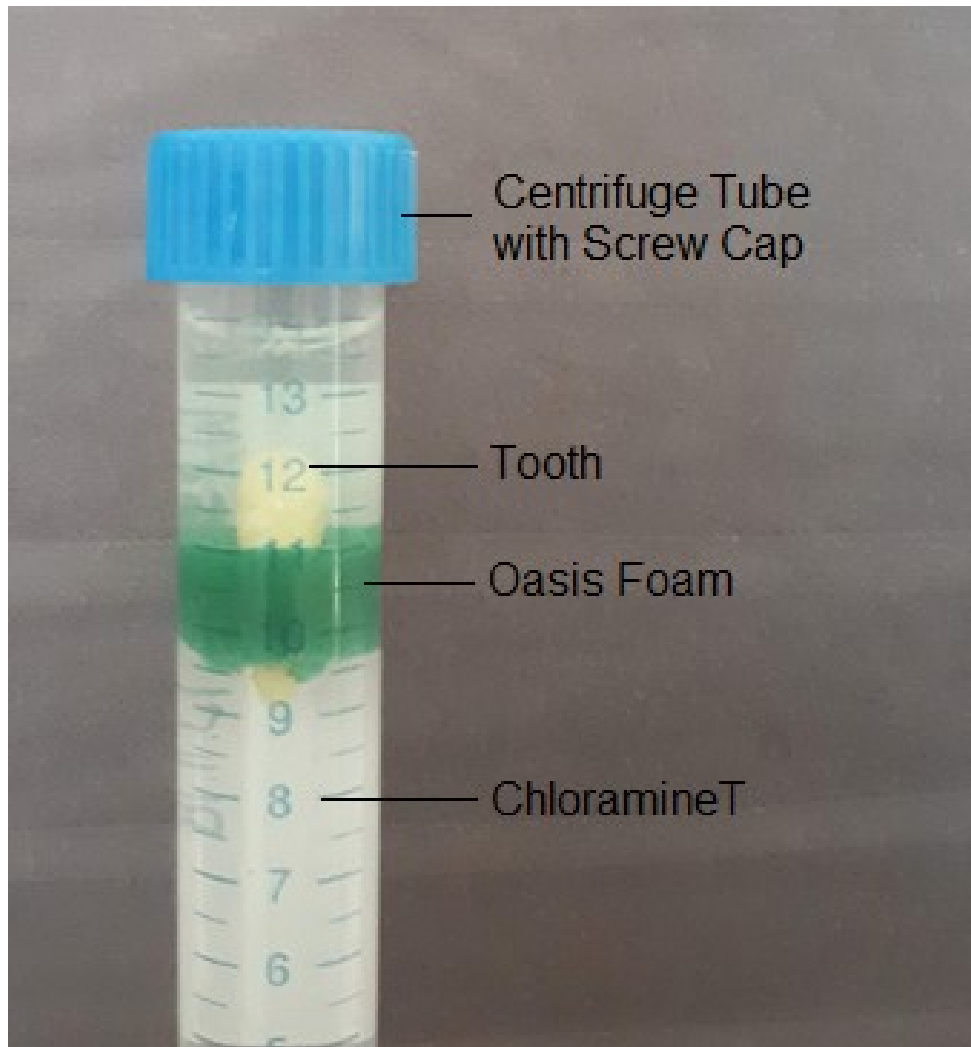


Fig. 7. Experimental setup for creating μ -CT images. Individual teeth were held in place with Oasis foam in a screw-capped centrifuge tube. The centrifuge tube was filled with 1% chloramine-T solution.

2.1.3 Experimental Setup: Photoacoustic Tomography (PAT)

For the pilot study, the MSOT inVision 128 (Multispectral Optoacoustic Tomography, iThera Medical GmbH; Munich, Germany; Fig. 8) was used to acquire PAT images. The MSOT inVision 128 can reach a spatial resolution of up to $150\ \mu\text{m}$ [84].



Fig. 8. MSOT inVision 128. **(Left)** The MSOT inVision 128 was used for the pilot study. **(Right)** For ultrasound detection, 128 toroidally focused ultrasound transducers organized in a concave array of 270-degree angular coverage were used. With permission from: <https://www.ithera-medical.com/products/msot-invision/>.

The device has a tunable optical parametric oscillator pumped by an Nd:YAG laser and can thereby provide excitation pulses with a duration of 9 ns at wavelengths ranging from 680 nm to 980 nm. The repetition rate is 10 Hz with a wavelength tuning speed of 10 m/s. The peak pulse energy is 100 mJ at 730 nm. Ten arms of a fiber bundle ensure the illumination of a ring-shaped light strip with a width of approximately 8 mm.

For ultrasound detection, 128 toroidally ultrasound transducers with a center frequency of 5 MHz (60% bandwidth) are used. These detectors are organized in a concave array of 270-degree angular coverage and a radius of curvature of 4 cm [84].

To generate PAT images, the MSOT inVision was filled with warm water (25°C) and the step size (distance between one picture to the next) was set to 0.3 mm. The individual tooth was held in place in a plastic film, which was attached to the holder. Water was used as coupling medium (Fig. 9a–b).



Fig. 9a. Experimental setup to create the photoacoustic images of the preliminary experiment. The tooth was held in a place in a plastic film attached to the holder and covered with water.

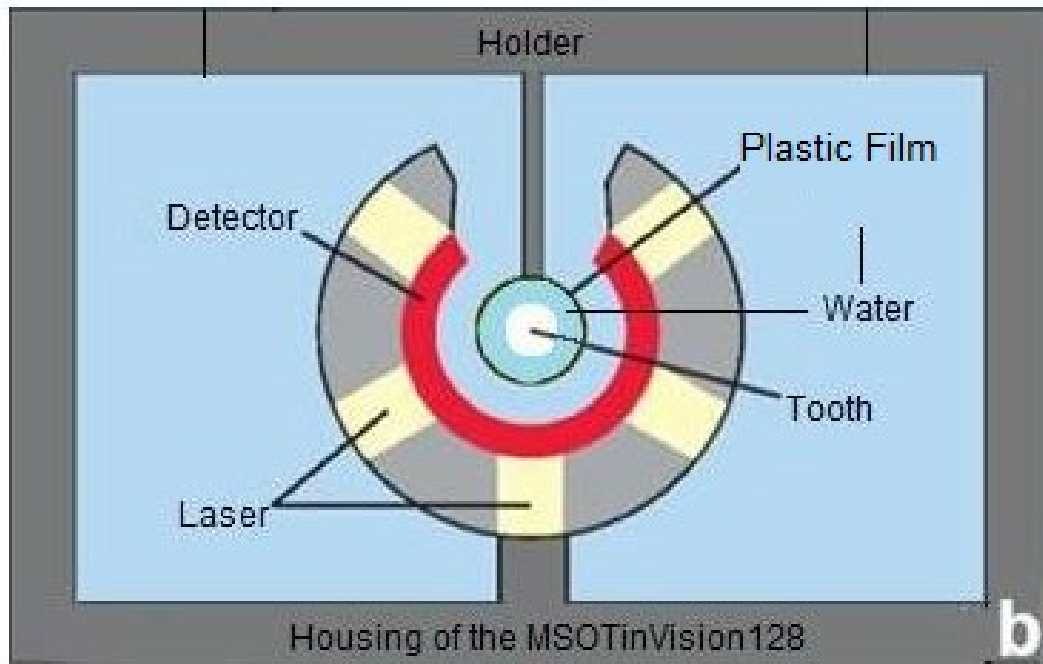


Fig. 9b. Experimental setup to create the photoacoustic images of the preliminary experiment. Schematic drawing of the interior components of the MSOT inVision, including the plastic film holder.

After being fixed in place, teeth were scanned at wavelengths of 680–960 nm, using 10 nm increments. PAT acquisition itself resulted in a stack of two-dimensional images of each tooth, which were saved as a TIFF file. After data acquisition, the images were analyzed. The imaging quality of each wavelength was assessed and compared with that of the others, which allowed the best wavelength to be identified. Thus, the use of 680 nm resulted in the best image quality when acquiring photoacoustic images of extracted human mandibular incisors.

2.1.4 Results of the Preliminary Experiment

For data analysis, the pilot study used the same approach as the main study (described in Chapter 2.2.5).

The average surface deviation between μ -CT and PAT imaging was determined to be 0.05 ± 0.06 mm. The average volume deviation was determined to be $15.70\pm 7.63\%$.

The size of the tooth affected the quality of the PAT, whereby image quality was better for smaller teeth than for larger ones. Consequently, mandibular incisors were used for the main study.

2.2 Experimental Setup of the Main Study

CBCT, μ -CT, and PAT were used in the main study.

Volumetric and surface accuracy was assessed, including calculation of minimum and maximum deviations.

2.2.1 Teeth

Ten intact and nine decayed extracted human, single-rooted incisors of the lower jaw were collected from patients with trauma or periodontitis. The selection of these teeth was based on the previous pilot study (Chapter 2.1).

After extraction, teeth were cleaned by means of an ultrasonic scaler (SONICflex LUX 2000L, KAVO; Biberach, Germany). Upon completion of cleaning, the teeth were stored for seven months in a 1% chloramine-T solution at 5°C.

2.2.2 Experimental Setup: Micro-Computed Tomography (μ -CT)

The experimental setup for generating μ -CT images was the same as that used in the pilot study (Chapter 2.1).

2.2.3 Experimental Setup: Cone-Beam Computed Tomography (CBCT)

For CBCT acquisition, the Orthophos XG 3D (Dentsply Sirona; York, PA, USA, Fig. 10) was used. The Orthophos XG 3D can reach a resolution of up to 80 μm [90].



Fig. 10. The Orthophos XG 3D (Dentsply Sirona; York, PA, USA).

Before CBCT imaging, teeth were fixed in place in a plastic holder (Fig. 11). This holder was specifically designed for this study in the software “Cubify Design” (3D Systems; Rock Hill, USA) and printed with the “German RepRap X350” three-dimensional printer (ccd systems; Berlin, Germany) using polyethylene terephthalate (PETG). A sketch of the holder is shown in Fig. 11.

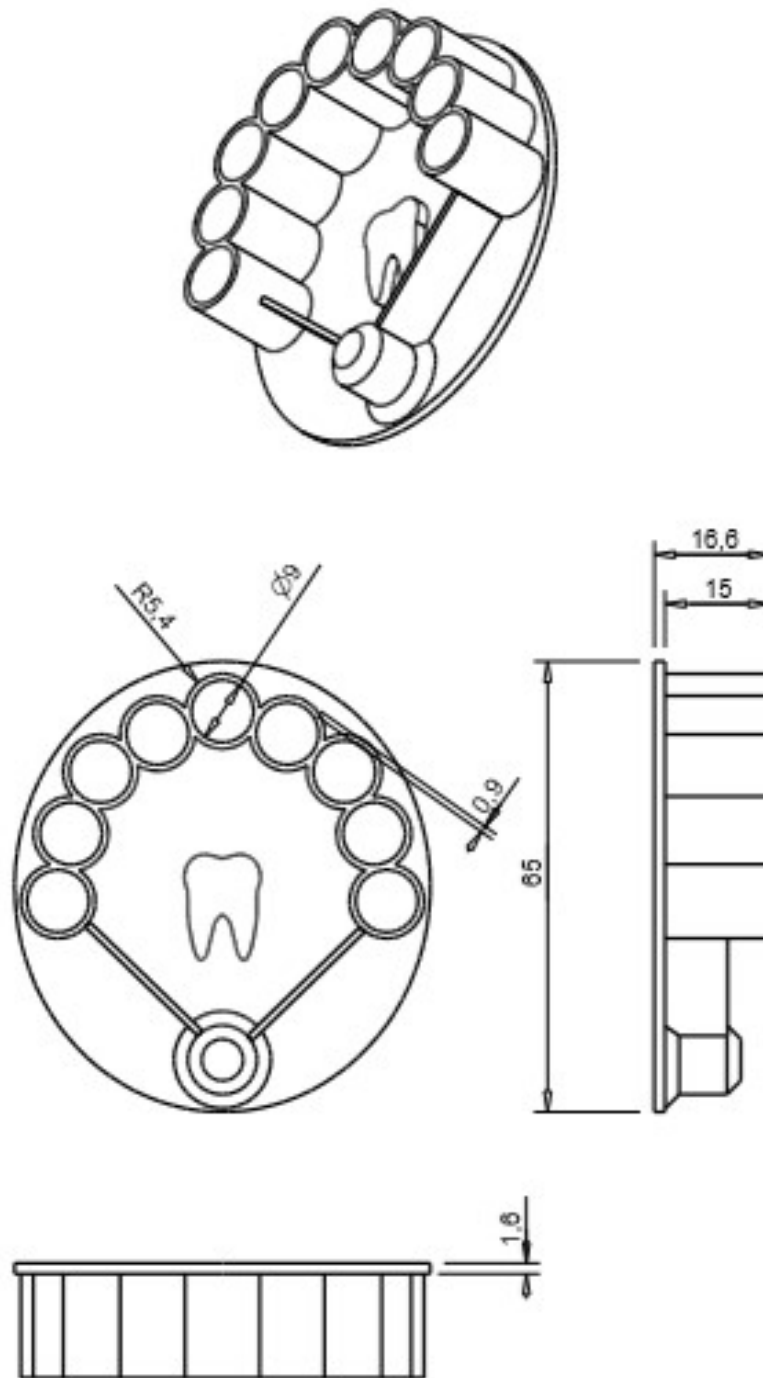


Fig. 11. Computer-aided design drawing of the plastic holder. The holder can be used to fix teeth in place for CBCT imaging. All dimensions are given in mm. R = radius. The drawing was designed in collaboration with another thesis supervised by Prof. Dr. Marc Schmitter.



Fig. 12. Experimental setup to create CBCT images. **(Left)** Overview image of the CBCT device and tripod. **(Right)** Detailed image of the tripod with plastic holder and teeth.

The holder was then placed on a tripod to achieve the right height (Fig. 12).

For image acquisition, the image acquisition parameters were set to high definition (voxel size 160 μm ; field of view $\text{Ø } 8 \times 8 \text{ cm}$). CBCT acquisition resulted in a stack of two-dimensional images of each tooth, which were saved as TIFF files.

2.2.4 Experimental Setup: Photoacoustic Tomography (PAT)

To improve the quality of the PAT images, some of the parameters applied in the pilot study were modified for the final study.

First, the MSOT inVision 256-TF was used instead of the MSOT inVision 128. The MSOT inVision 256-TF has twice as many detectors as the MSO inVision 128. Second, each tooth was embedded in a 20 ml plastic syringe, in a solution of 2% agarose with 1% lipofundin (Intralipid). The agarose was used to fix the tooth in a suitable position, and the lipofundin ensured better light scattering.

Fig. 13a shows how the tooth was fixed in the agarose and lipofundin mixture. Fig. 13b shows the MSOT inVision holder. A schematic drawing of the components of the MSOT is shown in Fig. 13c.

For PAT imaging, the MSOT inVision was filled with warm water (25°C), and the step size (distance between one picture to the next) was set to 0.3 mm. The imaging itself resulted in a stack of two-dimensional images of each tooth, and each image was saved as a TIFF file.

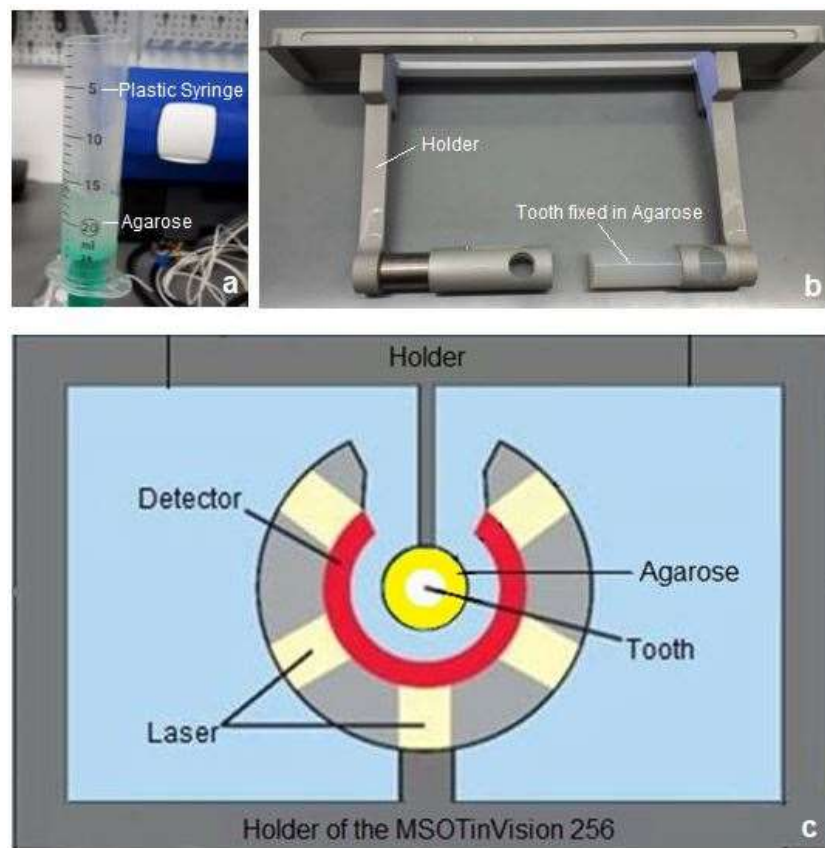


Fig. 13. Experimental setup for PAT images. **(a)** The tooth was embedded in an agarose and lipofundin solution in a plastic syringe. **(b)** Afterwards, the solidified agarose and lipofundin holder mixture was attached to the MSOT. **(c)** Schematic drawing of the interior components of the MSOT in Vision.

2.2.5 Data Analysis

μ -CT images served as the reference standard for the present study because the spatial resolution of μ -CT (up to 2 μm) is more accurate than that of CBCT (80 μm [90]) and PAT (150 μm [84]).

Both the root surface deviation (RSD) and volume deviation (VD) between the CBCT/PAT and μ -CT images were calculated and analyzed. To calculate RSD, the total average of the RSD (average of the positive and negative RSD values) was determined.

The acquired two-dimensional images (TIFF files) of the incisors were assembled and compiled into three-dimensional models by using version 4.10.1 of “3D Slicer,” a proprietary software program written in Matlab 2010b (MathWorks; Natick, Massachusetts, USA; Fig. 14).

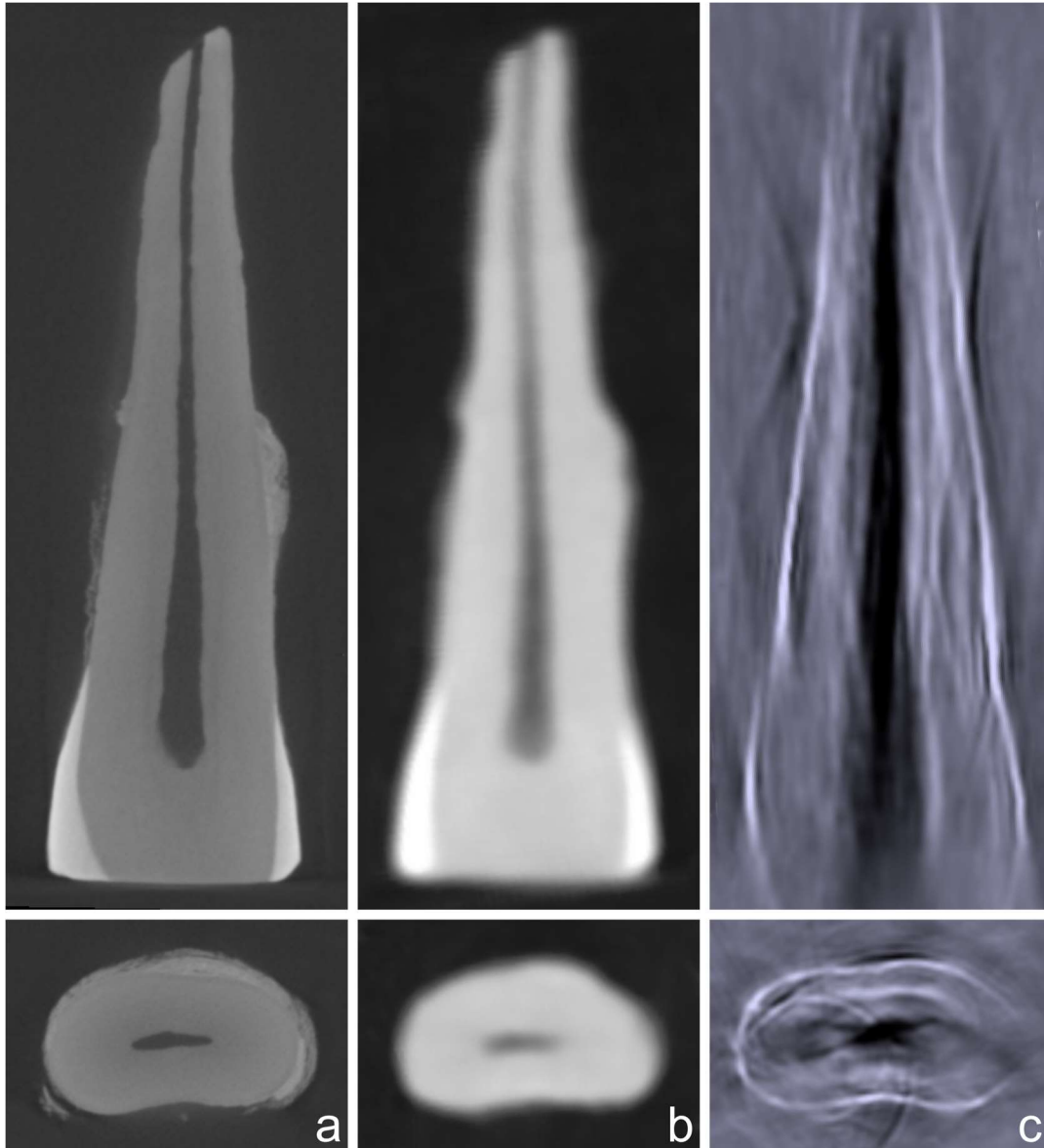


Fig. 14. Comparison of μ -CT, CBCT, and PAT images. The images show the longitudinal and transverse section of human mandibular incisors. (a) μ -CT image, (b) CBCT image, (c) PAT image.

Due to the inversion of the original data, the image of the three-dimensional μ -CT model was mirrored using the software Meshmixer 3.5.474 (Autodesk, Inc.). An example of a tooth before and after mirroring is shown in Fig. 15.

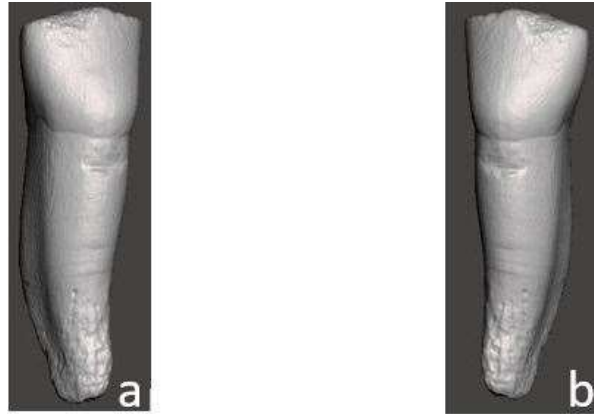


Fig. 15. Three-dimensional model of μ -CT image. **(a)** Back-to-front model. **(b)** Mirrored model by using software program Meshmixer 3.5.474 (017 Autodesk, Inc.).

The software program “GOM Inspect” (Braunschweig, Germany) was used to match and compare the three-dimensional models of each incisor. GOM Inspect has been certified by the Physikalisch-Technische Bundesanstalt (Braunschweig and Berlin, Germany) and the National Institute of Standards and Technology (Gaithersburg, Maryland, United States). Furthermore, the software matches images very precisely, producing the smallest surface deviation errors compared with other software programs [91]–[96].

The following standardized protocol was used when matching the images. First, GOM Inspect was used to match the CBCT images with the μ -CT images. Second, pre-alignment was carried out by selecting three points on the μ -CT manually. The first point marked the apex of the tooth, the second point marked the enamel–dentin junction, and the third point marked a prominent spot on the tooth crown. Afterwards, the corresponding points were marked on the CBCT model, and both images could be roughly aligned. To improve the accuracy of the matching process, a second alignment was carried out using GOM Inspect. Thus, the Gaussian matching method (Gaussian best-fit 3 sigma) was applied.

The same procedure was used for both the PAT and μ -CT images (Fig. 16).

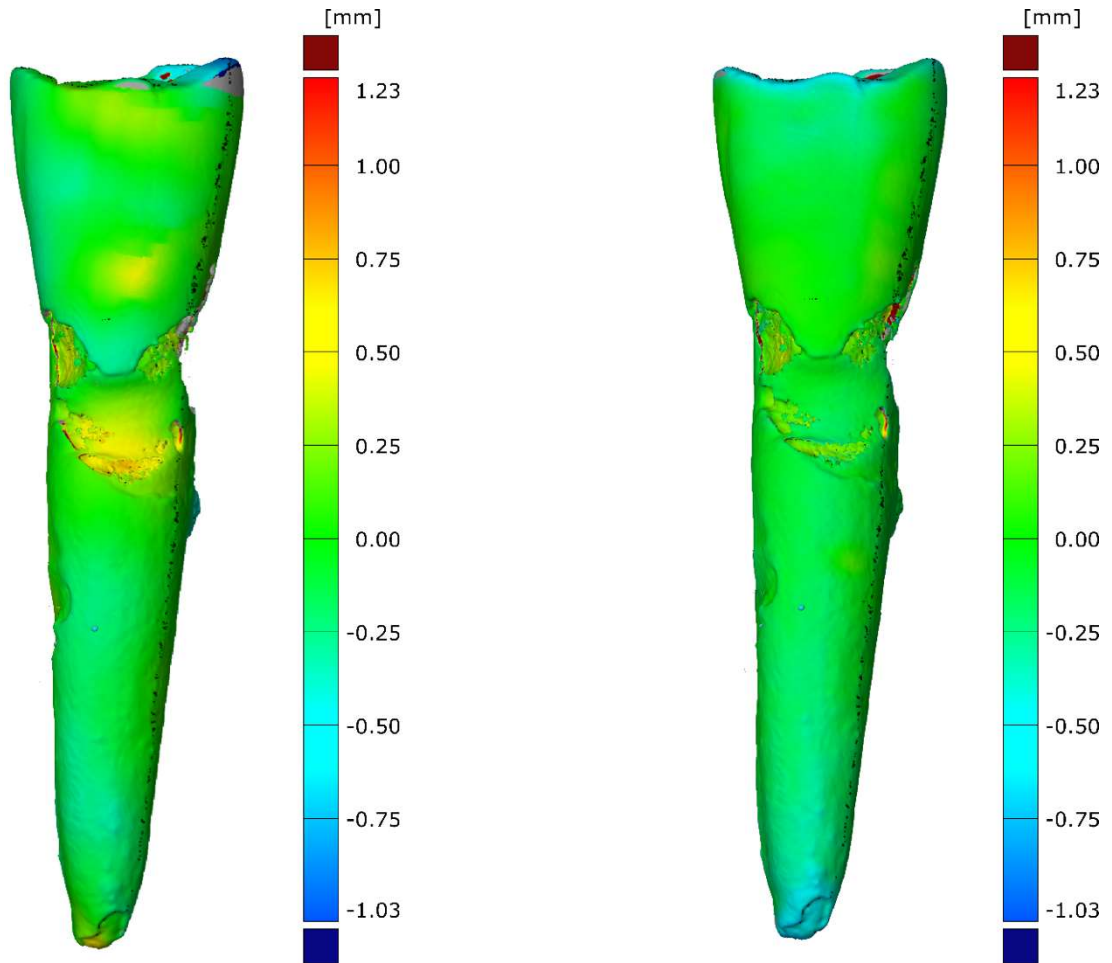


Fig. 16. Surface deviations of the three-dimensional models. **(Left)** PAT compared with μ -CT imaging. **(Right)** CBCT compared with μ -CT imaging.

Once the three-dimensional models had been matched, the total average of the deviation, the normalized total average of the deviation, the positive deviation, and the negative deviation of the root surface area (RSA) were calculated, using μ -CT as the reference standard.

In addition, the total volume of the root was determined and compared among the three models. The software program Fusion 360™ (2020 Autodesk, Inc.) was applied to crop the three-dimensional models of the same mandibular incisor to the same size. Afterwards, the volume of the root was calculated by applying the software program Meshmixer 3.5.474 (2017 Autodesk, Inc.).

The results of the matching process were displayed in a box-and-whisker plot. In this type of diagram (Fig. 17), the first and last 25% of the data are displayed as whiskers. The whisker of the first 25% is also called the first quartile (Q1; yellow), and the whisker of the last 25% is also called the third quartile (Q3; bright blue). The box/interquartile range (IQR; grey) describes the distance between the first and third quartile ($IQR = Q3 - Q1$) and hereby covers 50% of the data. The median (green) is placed in the box.

However, a whisker is never longer than 1.5 times the length of the box/IQR. If a value cannot be placed within the whisker, this value is marked as a statistical outlier (red circle).

The smallest value of the dataset that is not rated as an outlier is the minimum, and the largest value of the dataset that is not rated as an outlier is the maximum of the boxplot [97].

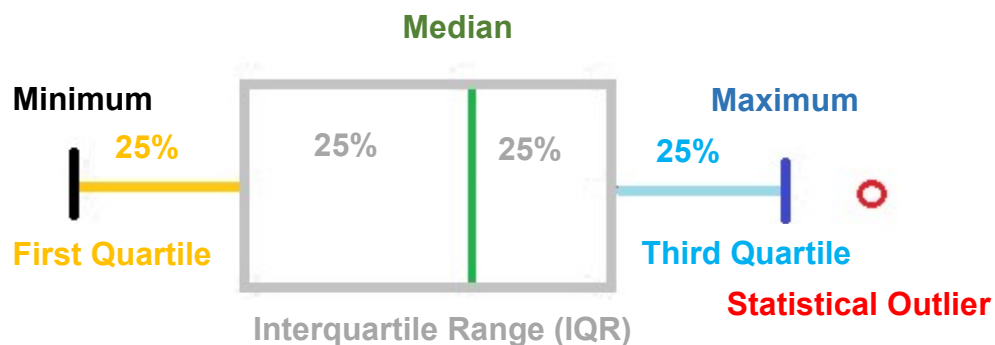


Fig. 17. Boxplot diagram. Minimum (**black**): the smallest data value excluding outliers. First quartile (**orange**): first 25% of the data. Box (**grey**): 50% of the data. Median (**green**): the median value of the dataset. Third quartile (**light blue**): last 25% of the data excluding outliers. Maximum (**dark blue**): the largest data value excluding outliers.

2.2.6 Statistical Evaluation

Data were analyzed in the software SPSS Statistics (Statistical Package for the Social Sciences, version 25.0.0; Armonk, USA). Several statistical tests were used, which are described in the following subsections.

2.2.6.1 Frequency Distribution

As a first step, the normal distribution of the data was analyzed using the Kolmogorov–Smirnov test. This test compares the observed cumulative distribution of scores with the theoretical cumulative distribution for a normally distributed population [98].

The results showed that seven out of ten groups had a normal distribution.

2.2.6.2 Significance Test

In the present study, a result is determined to be significant if the p-value is ≤ 0.05 and highly significant if the p-value is ≤ 0.01 [99].

In general, parametric and non-parametric tests can be used to determine the significance level. Parametric tests are used if the results are normally distributed. Non-parametric tests are used if the results are not normally distributed [100].

As mentioned, not every group showed a normal distribution. Therefore, a non-parametric test was applied to assess the significance level. For this purpose, the Mann–Whitney U test was applied.

The Mann–Whitney U test compares two mean values of random samples to calculate the significance level [101]. Therefore, all measured values of both groups were organized in a collective ranking list and for every value from “Group A,” it was counted how many values of “Group B” were ranked higher. At the end, the U value corresponds to the sum of the values that are ranked higher.

3 Results

The results for root volume and for the assessment of surface deviation are both presented in the following sections.

3.1 Total Volume Comparisons: Micro-Computed Tomography vs. Cone-Beam Computed Tomography vs. Photoacoustic Tomography (μ -CT vs. CBCT vs. PAT)

The total root volumes of the mandibular incisors are listed in a spreadsheet (Fig. 18), followed by three diagrams (Fig. 19–21) that visualize the results for each imaging modality.

Specimen	μ -CT (mm ³)	CBCT (mm ³)	PAT (mm ³)
1	141.97	146.89	108.58
2	132.99	112.16	119.61
3	134.13	117.85	135.29
4	210.79	184.46	224.59
5	166.62	150.01	176.82
6	150.25	137.25	138.32
7	112.95	99.76	109.94
8	128.48	122.21	118.94
9	146.91	141.78	126.94
10	80.97	72.24	73.57
11	98.25	92.12	94.02
12	133.31	103.10	115.35
13	168.67	148.98	168.39
14	151.14	133.88	136.98
15	84.85	80.10	59.01
16	215.37	184.88	235.87
17	88.32	80.52	78.85
18	217.66	190.35	199.74



Fig. 18. Total root volumes of mandibular incisors. Mandibular incisors were scanned in vitro by means of μ -CT, CBCT, and PAT.

3.1.1 Micro-Computed Tomography vs. Photoacoustic Tomography (μ -CT vs. PAT)

Comparing the μ -CT data with the PAT data yielded a mean total root volume of -7.33 mm^3 . The maximum deviation ranged between $+20.51 \text{ mm}^3$ and -33.40 mm^3 (Fig. 19).

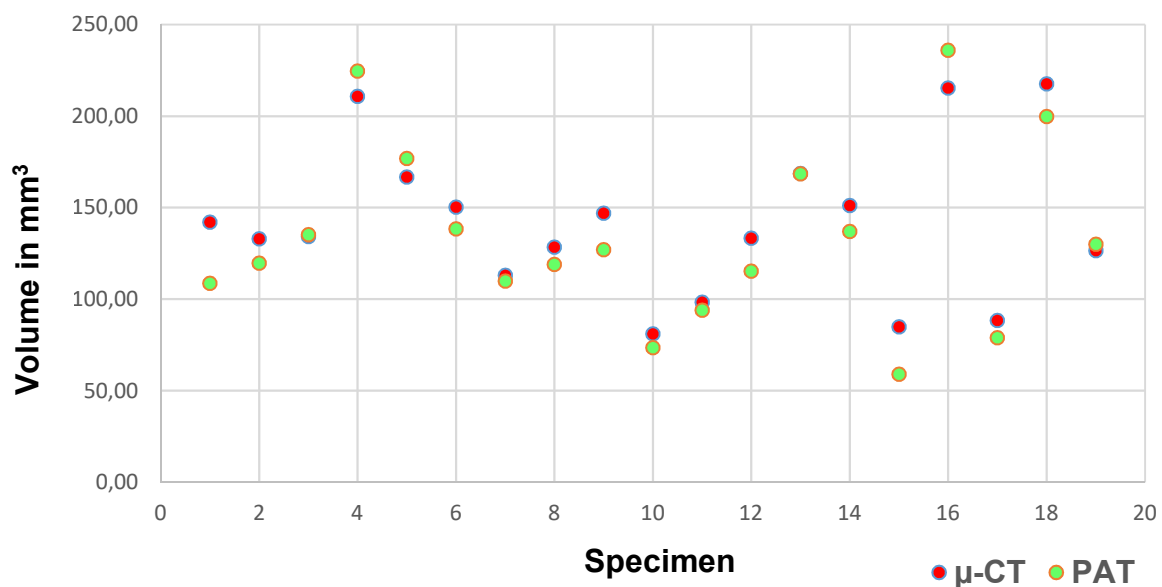


Fig. 19. Comparison of total volume (μ -CT vs. PAT). Mandibular incisors were scanned in vitro by means of μ -CT, CBCT, and PAT. Individual three-dimensional models were created and matched. The diagram shows the total root volume of the μ -CT models (red) compared with the PAT models (green).

3.1.2 Micro-Computed Tomography vs. Cone-Beam Computed Tomography (μ -CT vs. CBCT)

Comparing the μ -CT data with the CBCT data yielded a mean total root volume of -14.56 mm^3 . The maximum deviation ranged between $+4.91 \text{ mm}^3$ and -30.49 mm^3 (Fig. 20).

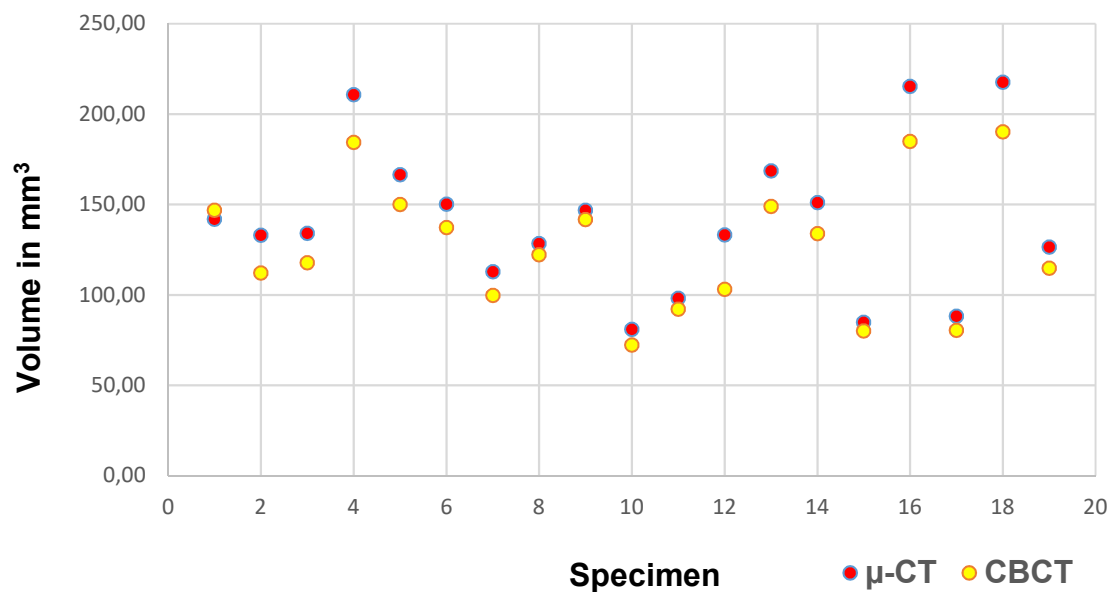


Fig. 20. Comparison of total volume (μ -CT vs. CBCT). Mandibular incisors were scanned in vitro by means of μ -CT, CBCT, and PAT. Individual three-dimensional models were created and matched. The diagram shows the total root volume of the μ -CT models (red) compared with the CBCT models (yellow).

3.1.3 Photoacoustic Tomography vs. Cone-Beam Computed Tomography (PAT vs. CBCT)

Comparing the PAT data with the CBCT data yielded a mean total root volume of 7.23 mm^3 . The maximum deviation ranged between $+51.00 \text{ mm}^3$ and -38.31 mm^3 (Fig. 21).

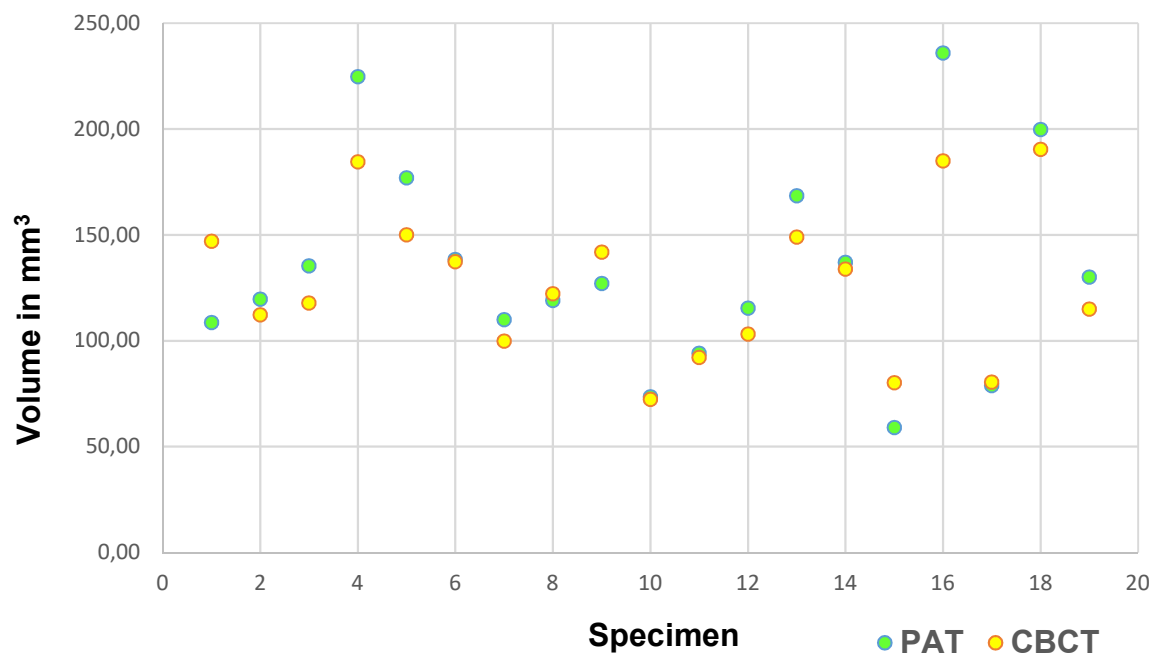


Fig. 21. Comparison of total volume (PAT vs. CBCT). Mandibular incisors were scanned in vitro by means of μ -CT, CBCT, and PAT. Individual three-dimensional models were created and matched. The diagram shows the total root volume of the PAT models (green) compared with the CBCT models (yellow).

3.2 Surface and Volume Deviations: Micro-Computed Tomography (μ -CT) vs. Cone-Beam Computed Tomography (CBCT) vs. Photoacoustic Tomography (PAT)

The surface and volume deviations among the μ -CT, CBCT, and PAT models of the mandibular incisors were calculated. The results of the surface and volume deviations were listed in a spreadsheet and organized into two groups. The first group shows the accuracy of PAT compared with μ -CT (Fig. 23 a, b, marked in white), and the second group shows the accuracy of CBCT compared with μ -CT (Fig. 23 a, b, marked in blue).

Fig. 22 defines the abbreviations used in Fig. 23 a, b.

PM	Total average of the deviation of the RSA (PAT compared with μ -CT)
CM	Total average of the deviation of the RSA (CBCT compared with μ -CT)
P (+)	Positive deviation of the RSA (PAT compared with μ -CT)
C (+)	Positive deviation of the RSA (CBCT compared with μ -CT)
P (-)	Negative deviation of the RSA (PAT compared with μ -CT)
C (-)	Negative deviation of the RSA (CBCT compared with μ -CT)
PN	Normalized total average of the deviation of the RSA (PAT compared with μ -CT)
CN	Normalized total average of the deviation of the RSA (CBCT compared with μ -CT)
PV	Volume deviation of the RSA (PAT compared with μ -CT)
CV	Volume deviation of the RSA (CBCT compared with μ -CT)
SD	Standard deviation

Fig. 22. List of abbreviations. Group 1: PAT vs. μ -CT (white); Group 2: CBCT vs. μ -CT (blue)

Specimen	PM (mm)	CM (mm)	Pplus (mm)	Cplus (mm)	Pminus (mm)	Cminus (mm)
1	-0.21	0.03	0.04	0.06	-0.25	-0.03
2	0.07	-0.05	0.12	<0.001	-0.05	-0.06
3	0.08	-0.05	0.17	0.06	-0.09	-0.11
4	0.03	-0.14	0.10	<0.001	-0.07	-0.15
5	0.04	-0.10	0.10	0.01	-0.06	-0.10
6	-0.02	-0.06	0.10	0.02	-0.12	-0.08
7	0.02	-0.07	0.10	0.03	-0.08	-0.10
8	-0.06	-0.02	0.07	0.03	-0.12	-0.05
9	-0.15	-0.03	0.03	0.02	-0.18	-0.05
10	-0.09	-0.10	0.05	0.01	-0.15	-0.10
11	-0.04	-0.08	0.06	0.01	-0.1	-0.08
12	-0.13	-0.21	0.03	<0.001	-0.16	-0.21
13	0.18	-0.09	0.22	<0.001	-0.05	-0.10
14	-0.04	-0.15	0.06	<0.001	-0.09	-0.16
15	-0.33	-0.06	0.01	<0.001	-0.33	-0.06
16	0.06	-0.17	0.13	<0.001	-0.07	-0.17
17	-0.09	-0.07	0.03	0.01	-0.12	-0.08
18	-0.09	-0.14	0.03	<0.001	-0.12	-0.15
19	0.06	-0.09	0.09	<0.001	-0.03	-0.09
SD	0.12	0.06	0.05	0.02	0.07	0.05
Mean	-0.04	-0.09	0.08	0.01	-0.12	-0.10

Fig. 23a. Surface and volume deviations for PAT compared with μ -CT, and for CBCT compared with μ -CT. Mandibular incisors were scanned using μ -CT, CBCT, and PAT. Individual three-dimensional models were created, and the μ -CT models were defined as the reference standard. CBCT and PAT images were compared with μ -CT images. The root surface and volume deviations between PAT and μ -CT, and between CBCT and μ -CT are displayed. (white) Deviations between μ -CT and PAT images. (blue) Deviations between μ -CT and CBCT images.

Specimen	PN (mm)	CN (mm)	PV (mm ³)	CV (mm ³)
1	-0.17	0.12	-33.40	4.91
2	0.11	0.04	-13.38	-20.84
3	0.12	0.04	1.16	-16.28
4	0.07	-0.05	13.80	-26.33
5	0.08	-0.01	10.21	-16.61
6	0.02	0.03	-11.93	-13.00
7	0.06	0.02	-3.01	-13.18
8	-0.02	0.07	-9.66	-6.27
9	-0.11	0.06	-19.96	-5.12
10	-0.05	-0.01	-7.40	-8.74
11	<0.001	0.01	-4.23	-6.13
12	-0.09	-0.12	-17.97	-30.21
13	0.22	<0.001	-0.28	-19.69
14	<0.001	-0.06	-14.17	-17.27
15	-0.29	0.03	-25.85	-4.75
16	0.10	-0.08	20.51	-30.48
17	-0.05	0.02	-9.46	-7.79
18	-0.05	-0.05	-17.91	-27.30
19	0.10	<0.001	3.55	-11.54
SD	0.12	0.06	13.58	9.65
Mean	<0.001	<0.001	-7.33	-14.56

Fig. 23b. Surface and volume deviations for PAT compared with μ -CT, and for CBCT compared with μ -CT. Mandibular incisors were scanned using μ -CT, CBCT, and PAT. Individual three-dimensional models were created, and the μ -CT images were defined as reference standard. CBCT and PAT images were compared with μ -CT images. The root surface and volume deviations between PAT and μ -CT, and between CBCT and μ -CT are displayed. (white) Deviations between μ -CT and PAT images. (blue) Deviations between μ -CT and CBCT images.

The results of the comparisons are shown in Fig. 24. The absolute values of the lower and the upper quartiles of the surface deviations were all $< \pm 0.15$ mm, and the median of the surface deviations was $< \pm 0.1$ mm. The absolute values of the lower and the upper quartiles of the volume deviations were all < -20 mm³, and the median of the volume deviations was < -13 mm³.

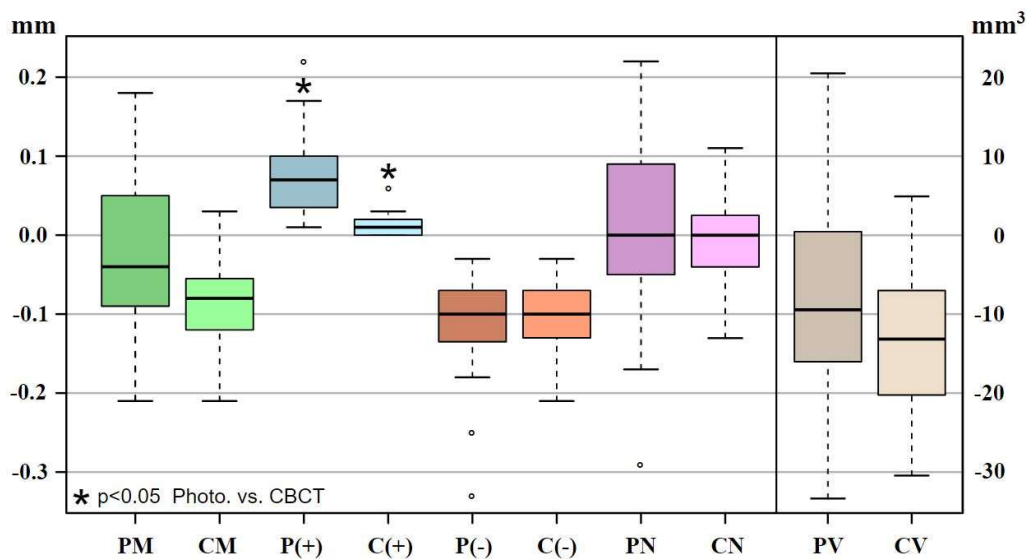


Fig. 24. Surface and volume deviations for PAT compared with μ -CT, and for CBCT compared with μ -CT. Mandibular incisors were scanned using μ -CT, CBCT, and PAT. Individual three-dimensional models were created. μ -CT images were defined as the reference standard. CBCT and PAT images were compared with μ -CT images. The root surface and volume deviations between PAT and μ -CT, and between CBCT and μ -CT are displayed. *= significant difference between PAT and CBCT. The results for the comparison of PAT with μ -CT have a slightly larger range than the results for the comparison of CBCT with μ -CT.

3.2.1 Photoacoustic Tomography vs. Micro-Computed Tomography (PAT vs. μ -CT)

For the comparison of PAT with μ -CT, the total average of the RSA (PM) ranged between -0.33 mm and 0.18 mm, with a mean of -0.04 and a standard deviation (SD) of 0.12 .

The normalized total average of the RSA (PN) ranged between -0.29 mm and 0.22 mm, with a mean of <0.001 and a SD of 0.12 .

The positive deviation of the RSA (Pplus) ranged between 0.01 mm and 0.22 mm, with a mean of 0.08 and a SD of 0.05 .

The negative deviation of the RSA (Pminus) ranged between -0.33 mm and -0.03 mm, with a mean of -0.12 and a SD of 0.07 .

The volume deviation of the RSA (PV) was also calculated. This ranged between 20.51 mm³ and -33.40 mm³, with a mean of -7.33 and a SD of 13.58 .

3.2.2 Cone-Beam Computed Tomography vs. Micro-Computed Tomography (CBCT vs. μ -CT)

For the comparison of CBCT with μ -CT, the total average of the RSA (CM) ranged between -0.21 mm and 0.03 mm, with a mean of -0.09 and a SD of 0.06 .

The normalized total average of the RSA (CN) ranged between -0.12 mm and 0.12 mm, with a mean of <0.001 and a SD of 0.06 .

The positive deviation of the RSA (Cplus) ranged between <0.001 mm and 0.06 mm, with a mean of 0.01 and a SD of 0.02 .

The negative deviation of the RSA (Cminus) ranged between -0.21 mm and -0.03 mm, with a mean of -0.10 and a SD of 0.05 .

In addition to the determination of RSA, the volume deviation of the RSA was calculated (CV). This ranged between 4.91 mm³ and -30.48 mm³, with a mean of -14.56 and a SD of 9.65 .

3.2.3 Photoacoustic Tomography vs. Cone-Beam Computed Tomography (PAT vs. CBCT)

The Mann–Whitney U test was applied to compare the results of the PAT and CBCT groups. The total average of the RSA showed no significant difference between the two imaging techniques ($p=0.06$). Both the negative average of the RSA ($p=0.64$) and the results of the volume deviation ($p=0.11$) showed no significant difference between PAT and CBCT.

The results of the positive deviation of the RSA (PAT compared with CBCT) showed a significant difference ($p<0.001$; Fig. 25).

	p-value	
PM vs. CM	0.06	No significant difference
Pplus vs. Cplus	<0.001	Significant difference
Pminus vs. Cminus	0.64	No significant difference
PN vs. CN	0.79	No significant difference
PV vs. CV	0.11	No significant difference

Fig. 25. PAT vs. CBCT (Mann–Whitney U test). The comparison showed no significant differences between the two groups, with the exception of the results for the positive deviation of the RSA (PAT compared with CBCT).

4 Discussion

In contrast to US and OCT, PAT utilizes both light and sound to generate an image. If only light is used (see OCT), the penetration depth is quite limited, due to scattering in the tissue. If only ultrasound is used (see US), a better penetration depth can be achieved, due to a reduction in the scattering effect. However, the application of US results in a poor contrast [87]. The detour from light to sound that occurs in PAT achieves both a higher spatial resolution and a greater penetration depth than OCT or US [23]. However, the spatial resolution of PAT is still limited, because it is affected by various other factors: it is compromised by acoustic inhomogeneity, a lack of sufficient data (due to a limited view angle), and a limited bandwidth of the detection system caused by the size of the detector aperture [102].

Nonetheless, the spatial resolution of PAT is already sufficient to achieve reliable information about early-stage caries, as was shown by a 2016 in-vitro study by Cheng et al. [103]. This finding was supported by Koyama et al., who showed in 2018 that it might be possible to use PAT for the detection of caries. In that study, caries could be detected by using frequency components of 0.5–1.2 MHz on specimens with simulated caries. In caries-free specimens, however, this frequency was not adequate [104].

Because PAT measurements are associated with an increase in temperature in the illuminated tissue, care must be taken to ensure that the pulp of the examined tooth remains undamaged. In an in-vitro study in 2006, Li and Dewhurst showed that the temperature of a postmortem tooth does not increase by more than 5°C during PAT measurement. This is important information, because Li and Dewhurst found that the pulp starts to necrotize if it is heated by more than 5°C. Furthermore, Li and Dewhurst demonstrated that it is possible to assess the distribution of caries in postmortem dental samples by using PAT [105].

4.1 Accuracy of PAT

The present study assessed the accuracy of PAT and CBCT data for dental imaging. For this purpose, PAT and CBCT volume and surface data were compared with corresponding data from μ -CT, which served as the reference standard. Afterwards, the individual deviations between μ -CT and both PAT and CBCT were compared. For this purpose, extracted mandibular incisors were scanned in vitro using PAT, CBCT, and μ -CT. Subsequently, three different three-dimensional models, one for each imaging technique, were created for each tooth. Finally, the three different three-dimensional models acquired from the same tooth were matched and analyzed regarding volume and surface.

By comparing these three different models, it was shown that the results for the comparison of PAT with μ -CT had a wider range than the results for the comparison of CBCT with μ -CT (Fig. 24). This might be because the ultrasound detection array of the MSOT inVision has an angular convergence of only 270 degrees, whereas CBCT has 360-degree angular coverage.

Because teeth were embedded in water and agarose, it was not possible to reliably prevent the teeth from moving during scanning, which might have led to movement artifacts in some cases.

The penetration depth of x-rays is superior to that of near-infrared light, resulting in lower-quality images when PAT is used. This fact is of special interest regarding teeth that have e.g. a thicker layer of root cementum: the light will not be able to penetrate these teeth as easily as teeth with a thin layer of root cementum.

Imaging of the pulp was associated with larger volume deviations in PAT than in μ -CT and CBCT. Because the pulp is located in the center of the tooth, the light might have been reflected while crossing the enamel and dentin layers. This might explain the inaccuracies in PAT with respect to the volume of the pulp chamber.

Nonetheless, the comparison of the results for PAT– μ -CT and CBCT– μ -CT showed that the surface and volume deviations were not significant, except for the subcategory Pplus/Cplus. Although the differences in this subgroup were

significant, the maximum absolute difference was only 0.22 mm, which is not important from a clinical point of view.

4.2 PAT for Daily Clinical Practice in Dentistry

In an in-vitro study in 2005, Jeleva et al. demonstrated that it is possible to detect the absence or presence of liquids under ceramic crowns by using PAT [48].

In their 2006 in-vitro study, El-Sharkawy et. al. used a Nd:YAG laser with a wavelength of 1064 nm to examine the optical and physical properties of teeth. They showed that it is possible to distinguish between an intact and a decayed tooth by calculating the longitudinal sound speed, optical penetration depth, and Grueneisen coefficient of the tooth [106].

In 2010, Li and Dewhurst [105] showed that the temperature increase during PAT imaging remains below the safety limit of 5°C. This means that photoacoustic imaging causes no physical damage to the tissue of the tooth. Furthermore, it was shown that PAT provides high sensitivity regarding the detection of early-stage caries. For this purpose, three-dimensional and two-dimensional models were designed based on PAT images. However, PAT was not compared with a reference standard [105].

Moore et al. demonstrated in 2018 that it is possible to depict the gum, gingival margin, and gingival thickness of teeth 7–10 and 22–27 by using PAT in combination with a contrast medium (cuttlefish ink). Furthermore, the study showed that PAT provides a more reliable measurement of periodontal pocket depths than a dental hygienist using a periodontal probe [107].

All these studies came to the conclusion that PAT is suitable for imaging teeth and the surrounding tissue. However, to the best of the author's knowledge, the present study is the first to show that PAT imaging is almost as accurate as CBCT imaging concerning surface and volume deviations.

4.3 PAT Compared With Other Non-Ionizing Imaging Techniques

Many other non-ionizing imaging techniques such as US, MRI, and OCT are available. Because PAT has to compete with these imaging techniques, it is useful to discuss some recent findings for US, MRI, and OCT in relation to dentistry, in order to rank the value of PAT in this context.

4.3.1 Ultrasound

In his review, Marotti et al. presents 58 articles about the use of US in dentistry [108]. The results of the most interesting papers in this review are described in the following.

Slak et al. showed that the thickness of enamel can be assessed with adequate accuracy [109].

On the basis of three test persons, Salmon et al. demonstrated that US can be used in vivo to visualize dental implants, periodontal structures, and even a mucocele [110].

In their study comparing US images with bitewing radiographs, Matalon et al. found that that US had a specificity of 0.92 and a sensitivity of 0.9 with respect to the detection of carious lesions [111].

4.3.2 MRI

A study by Kress et al. showed that the image resolution of MRI is sufficient to depict the temporomandibular joint and to evaluate the integrity of the inferior alveolar nerve [112].

In another study, the same research group revealed that MRI is even able to depict the teeth. Furthermore, Kress et. all showed that, by measuring the blood flow within the pulp of teeth, MRI can be used to differentiate between young (27 years or less) and old (48–77 years) teeth [113].

4.3.3 OCT

Fried et al. showed that cracks in teeth are easily visible in both *in vivo* and *in vitro* images in OCT at wavelengths around 1300 nm [74].

In another in-vivo study, Chan et al. were able to measure the internal structure and depth of carious lesions in 62 out of 63 teeth using a wavelength of 1300 nm [114].

An in-vivo study by Shimada et al. demonstrated that OCT images are more accurate and reliable for the detection of enamel lesions and dentin caries than conventional bitewing radiographs [115].

4.4 PAT for Daily Clinical Practice in Other Medical Applications

In addition to dentistry, PAT is becoming increasingly important in other medical applications. These are presented in the following sections.

4.4.1 Brain Imaging

Imaging the brain using PAT remains challenging, because the skull and brain tissue of larger mammals such as monkeys generate strong optical scattering. This scattering severely limits optical fluency [116]. Imaging the brains of smaller mammals such as rodents is less challenging. Because they have thin skulls, PAT has been used in multiple in-vivo studies to image the brains of small animals [117], [118].

4.4.2 Thyroid Imaging

Existing imaging methods such as scintigraphy, CT, PET-CT, and MRI lack the specificity to distinguish between malignant and benign follicular nodules in thyroid tissue. Therefore, thyroid cancer is diagnosed by using US in combination with invasive needle aspiration cytology, followed by a histological evaluation. In this context, the difficulty in diagnosing thyroid cancer should be kept in mind;

namely, conventional primary diagnostics are sensitive but do not allow differentiation between aggressive lesions and subclinical cancers, leading to overdiagnosis and overtreatment. In contrast, the location and anatomic structure of the thyroid gland means it is a good candidate for PAT imaging. Thus, PAT might be a promising imaging technique once a suitable imaging contrast (either exogenous or endogenous) is found [118]–[122].

4.4.3 Breast Imaging

Another promising domain for the use of PAT is breast imaging. In the female breast, most of the targeted tissues are located superficially and can therefore be imaged. Furthermore, healthy breast tissue has a low optical absorption and scattering, whereas abnormally increased vasculature [123] and hemoglobin at tumor sites produces an intense photoacoustic signal.

However, breast imaging by use of PAT remains challenging. Clinical PAT systems are in the process of being improved further, which will enable breast lesion detection in a regular clinical setting [118].

4.4.4 Dermatological Imaging

The gold standard remains invasive biopsies combined with histopathological analysis, even though the skin is easily accessible [118] and some optical imaging systems, such as OCT or high-frequency ultrasonography, are already in use. However, OCT shows a distinct limitation with respect to penetration depth (1–2 mm), and high-frequency US lacks molecular and functional imaging capabilities [124]. PAT could perform significantly better in both of these areas and could be used for dermatological imaging. Nevertheless, a single “all-rounder PAT application” is not yet available. One reason could be the need for direct physical tissue contact [118].

4.5 Outlook for PAT in Daily Clinical Practice

The results of the presented and previous studies indicate that PAT promises to be a highly valuable diagnostic tool in various medical fields. In contrast to other common imaging techniques, PAT has the advantage of utilizing non-ionizing laser light, which makes it a portable technique. PAT allows the detection of endogenous chromophores, such as hemoglobin and melanin, without the need to inject exogenous molecular imaging agents. In addition, PAT devices are becoming more and more affordable due to cheaper ultrasound and laser components [23]. However, this innovative imaging technique still needs to be improved to enable its application in daily clinical practice. In particular, its spatial resolution and penetration depth in some tissues and some specific anatomic locations have to be improved. In this context, the penetration of bone, air, and voluminous teeth poses problems that have to be solved.

Therefore, further developments of PAT would be desirable, for example, a detector with a concave array of 360-degree angular coverage, to avoid blurring at the top of photoacoustic images and to enhance spatial resolution.

Furthermore, it would be useful to develop an improved algorithm to transfer the gathered dental data into an image. A modified algorithm would be especially useful for the PAT examination of hard tissue, because the algorithm currently used by the MSOT inVision is predominately designed for imaging soft tissue.

In summary, the hypothesis of the present study has to be partially rejected because there were significant differences between PAT and μ -CT with respect to the positive surface deviation of mandibular human incisors. However, with respect to the other variables assessed in the present study, no significant differences could be found.

4.6 Study Limitations

The in-vitro nature of this study means its results must be interpreted with some caution. However, because the teeth are surrounded by bone, it would have been

very challenging to assess them in vivo. The present study aimed to provide a basis for further clinical studies; thus, the in-vitro approach used in this study to obtain preliminary results is justified. Furthermore, the size of human teeth differs from molars to incisors. In the present study, mandibular incisors were used due to their smaller size. The results therefore cannot be extrapolated without reservation to human molars, for example.

Finally, the results of the present study with respect to PAT are based on the MSOT inVision 256-TF device. Consequently, the results cannot be directly transferred to other PAT devices.

5 Summary

Because three-dimensional images have a substantial impact on diagnosis, treatment planning and, consequently, the success rate of medical treatment, high-resolution imaging and three-dimensional reconstruction of teeth in dentistry have gained fundamental importance.

Despite the availability of non-ionizing imaging techniques, x-ray imaging is still used as standard in dentistry. For this reason, this study examined and compared the accuracy of the newly emerging imaging technique PAT with that of μ -CT as the established, reference standard imaging technique. Three-dimensional models were created, based on PAT, CBCT, and μ -CT data. To collect the data, each imaging technique was used to scan human mandibular incisors. Because the μ -CT models were defined as the gold standard, the three-dimensional PAT and CBCT models were compared with the three-dimensional model of the μ -CT data. In addition, both groups (PAT- μ -CT and CBCT- μ -CT) were compared with each other.

The present study demonstrated that PAT can already be used to make accurate reconstructions of the root surface and volume of mandibular incisors.

In general, the surface deviations between the PAT and μ -CT images were slightly larger than the surface deviations between the CBCT and μ -CT images. The difference between the PAT- μ -CT group and the CBCT- μ -CT group

regarding the total average of the RSA was not found to be significant ($p=0.06$). However, the maximum positive deviation between the PAT and μ -CT images was 0.18 mm, and the maximum negative deviation was -0.33 mm. In clinical daily practice, these discrepancies are of negligible importance.

Although the comparison of dental root volume showed that PAT and CBCT images had a slightly smaller volume than the μ -CT images, these differences were not significant ($p=0.11$).

It can be concluded that three-dimensional reconstructions based on in-vitro PAT can already achieve an acceptable reconstruction quality. Nevertheless, further research is necessary to improve the accuracy of PAT imaging, especially when it comes to in-vivo imaging. Here, the imaging of teeth, and especially their roots, is considerably complicated, because the root is covered by bone that has to be penetrated by light when using PAT.

Due to the fact that this imaging technique is still in its infancy and the algorithm used to calculate the images is designed for soft tissue, it can be stated that the ability to use the photoacoustic effect to show molecular and optical contrasts will lead to a valuable diagnostic tool in the future.

6 Appendix

6.1 Materials

6.1.1 Equipment

μ -CT	MetRIC (Micro and region of interest CT)	Designed and constructed by the Institute for X-ray Microscopy, Fraunhofer IIS Wuerzburg, Bavaria, Germany
CBCT	Orthophos XG 3D	Dentsply Sirona, York, PA, USA
PAT	MSOT inVision 256-TF	iThera Medical, Munich, Germany
3D printer	GermanRepRapX350	German RepRap GmbH Feldkirchen, Germany
Ultrasonic scaler	SONICflex LUX 2000L	KAVO, Bieberach, Germany

6.1.2 Consumables

Oasis		Gravidus GmbH, Bremen, Germany
Falcon Tube (15 ml)		Sigma-Aldrich Chemie GmbH, Taufkirchen, Germany
Disposable syringe		

	B. Braun Deutschland GmbH & Co. KG, Melsungen, Germany
PETG (polyethylene terephthalate)	Filamentworld, Neu-Ulm, Germany
Plastic wrap	allpack24, Nersingen, Germany

6.1.3 Solutions

Chloramine-T solution 1 g solution contains 10 mg chloramine-T (= tosylchloramide sodium) SAP Nr. 712170	Pharmacy of Wuerzburg University Hospital Innere Aumühlstraße 3 97076 Wuerzburg Germany
Lipofundin MCT 20%	B. Braun Melsungen AG 34209 Munich Germany
Agarose Standard Item nr. 3810.3 Batch 147257100	Carl Roth GmbH + Co. KG Schoemperlenstr. 3–5 76185 Karlsruhe Germany

6.1.4 Software

3D Slicer 4.10.1 r27931	National Alliance for Medical Image Computing (NA-MIC) Funded by the National Institutes of Health through the NIH Roadmap for Medical Research, Grant U54 EB005149	
Meshmixer 3.5.474	©2017 Autodesk, Inc., San Rafael, USA	
GOM Inspect 2018	(2018 Hotfix 5, Rev. 115656, Build 2019-02-15) Tested and certified by NIST (National Institute of Standards and Technology, Gaithersburg, Maryland, USA) and PTB (Physikalisch-Technische Bundesanstalt, Braunschweig and Berlin, Germany)	
Cubify Design	3D Systems, Rock Hill, South Carolina, USA	
SPSS Statistics Statistical Package for the Social Sciences, version 25.0	IBM Deutschland GmbH IBM-Allee 71139 Ehningen Germany	1
Fusion 360™ 2.0.8816	©2020 Autodesk, Inc., San Rafael, USA	

6.2 Reference List

- [1] R. Pauwels, "History of Dental Radiography: Evolution of 2D and 3D Imaging Modalities," *Med. Phys. Int. J.*, no. Special Issue, History of Medical Physics 3, pp. 235–277, 2020.
- [2] J. Dicker, "Röntgendiagnostik mit der Panorama-Schicht-Aufnahme," pp. 20, 47–75, 2000.
- [3] B. Partik, P. Pokieser, and G. T. Zubehör, *Die Intensivmedizin*. 2011.
- [4] R. Schulze *et al.*, "Dentale Volumentomographie (DVT). – S1-Empfehlung," *DGZMK*, vol. 64, pp. 490 – 496, 2009.
- [5] M. Stimmelmayer *et al.*, "Accuracy and reproducibility of four cone beam computed tomography devices using 3D implant-planning software," *Int. J. Comput. Dent.*, vol. 20, no. 1, pp. 21–34, 2017.
- [6] M. Karbownik and R. J. Reiter, "Antioxidative Effects of Melatonin in Protection Against Cellular Damage Caused by Ionizing Radiation," *Proc. Soc. Exp. Biol. Med.*, vol. 225, no. 1, pp. 9–22, 2008.
- [7] "Die Forschung , die zum Nobelpreis führte Arbeiten und Leben in Würzburg Wilhelm Conrad Röntgen," *Julius-Maximilians-Universität Würzburg*, 2020. [Online]. Available: <https://www.physik.uni-wuerzburg.de/ueber-uns/fakultaetsgeschichte/nobelpreistraeger/wilhelm-conrad-roentgen/>.
- [8] H. Schild, "Röntgenstrahlen in der Radiologischen Diagnostik," 2018. [Online]. Available: http://www.uni-bonn-radiologie.de/front_content.php?idart=430.
- [9] W. Alberti and G. Politzer, "Über den Einfluss der Röntgenstrahlen auf die Zellteilung.," *Springer-Verlag*, p. 284, 1924.
- [10] W. Scholtz, "Über den Einfluss der Röntgenstrahlen auf die Haut in gesundem und krankem Zustande," *Springer-Verlag*, vol. 59, no. 3, pp. 421–446, 1902.
- [11] F. Angelieri, G. R. de Oliveira, E. Sannomiya, and D. A. Ribeiro, "DNA damage and cellular death in oral mucosa cells of children who have undergone panoramic dental radiography," *Pediatr. Radiol.*, vol. 37, no. 6,

- pp. 561–565, 2007.
- [12] “BfS - Röntgen - Röntgendiagnostik: Häufigkeit und Strahlenexposition,” *Bundesamt für Strahlenschutz*, 2020. [Online]. Available: <https://www.bfs.de/DE/themen/ion/anwendung-medizin/diagnostik/roentgen/haeufigkeit-exposition.html>.
- [13] “Bundesamt für Strahlenschutz Grafik.pdf,” 2020. [Online]. Available: <https://www.bfs.de/DE/themen/ion/anwendung-medizin/diagnostik/roentgen/haeufigkeit-exposition.html>.
- [14] I. Peroz, “Das Kiefergelenk ins rechte Bild gerückt,” *zm-online*, no. 22, p. 14,17, 2013.
- [15] Federal Republic of Germany, “Strahlenschutzgesetz (StrlSchG),” *Bundesgesetzblatt (BGBl)*, vol. Section 83, no. paragraph 3, third sentence, p. 1966.
- [16] P. I. Wang *et al.*, “Imaging of Pregnant and Lactating Patients,” *Am. J. Roentgenol.*, vol. 198, no. 4, pp. 778–784, 2012.
- [17] D. W. McRobbie, E. A. Moore, and M. J. Graves, “MRI from picture to proton,” *MRI from Pict. to Prot.*, pp. 109–117, 2017.
- [18] H. Venables, “How does ultrasound work?,” *Ultrasound*, vol. 19, no. 1, pp. 44–49, 2011.
- [19] A. Girach and R. C. Sergott, “Optical Coherence Tomography,” p. 2, 2016.
- [20] M. Machoy, J. Seeliger, L. Szyszka-Sommerfeld, R. Koprowski, T. Gedrange, and K. Woźniak, “The Use of Optical Coherence Tomography in Dental Diagnostics: A State-of-the-Art Review,” *J. Healthc. Eng.*, vol. 2017, pp. 1–2, 2017.
- [21] S. R. Ghorayeb and T. Valle, “Experimental evaluation of human teeth using noninvasive ultrasound: Echodentography,” *IEEE Trans. Ultrason. Ferroelectr. Freq. Control*, vol. 49, no. 10, pp. 1437–1443, 2002.
- [22] M. Schmitter, O. Gabbert, B. Ohlmann, and A. Hassel, “ORAL AND MAXILLOFACIAL RADIOLOGY Editor : Allan G . Farman Assessment of the reliability and validity of panoramic imaging for assessment of mandibular condyle morphology using both MRI and clinical examination

- as the gold standard,” vol. 102, no. 2, pp. 220–224, 2006.
- [23] S. Zackrisson; S.M.W.Y. van de Ven; S.S. Gambhir, “Light In and Sound Out Emerging Translational Strategies.pdf,” p. 979, 2014.
- [24] H. Kobayashi, M. Ogawa, R. Alford, P. L. Choyke, and Y. Urano, “New Strategies for Fluorescent Probe Design in Medical Diagnostic Imaging,” *Chem. Rev.*, vol. 110, no. 5, pp. 2620–2640, 2010.
- [25] H. E. Schroeder, “Orale Strukturbiologie 95,” p. 95, 1982.
- [26] J. R. Zijp and J. J. Bosch, “Theoretical model for the scattering of light by dentin and comparison with measurements,” vol. 32, no. 4, p. 412, 1993.
- [27] H. E. Schroeder, “Orale Strukturbiologie,” p. 145, 1982.
- [28] H. E. Schroeder, “Orale Strukturbiologie,” p. 129, 1982.
- [29] L. He, “Mechanical behaviour of human enamel and the relationship to its structural and compositional characteristics (doctorate thesis).,” *Biomater. Sci. Res. Unit. Fac. Dent. Univ. Sydney*, no. May, p. 11, 2008.
- [30] E. Hellwig, J. Klimek, and T. Attin, *Einführung in die Zahnerhaltung*, 3rd ed. Urban & Fischer Verlag/Elsevier GmbH; Auflage: 3 (10. April 2003), 2003.
- [31] H. E. Schroeder, “Orale Strukturbiologie,” p. 73, 1982.
- [32] H. E. Schroeder, “Orale Strukturbiologie,” pp. 87–88, 1982.
- [33] B. Yeom *et al.*, “Abiotic tooth enamel,” *Nature*, vol. 543, no. 7643, pp. 95–98, 2017.
- [34] H. E. Schroeder, “Orale Strukturbiologie,” p. 75, 1982.
- [35] G. Duplain and R. Boulay, “Complex index of refraction of dental enamel at CO₂ laser wavelengths,” *Appl. Opt.*, vol. 26, no. 20, p. 4447, 1987.
- [36] P. Gängler, T. Hoffmann, B. Willershausen, N. Schwenzer, and M. Ehrenfeld, “Konservierende Zahnheilkunde und Parodontologie,” p. 34, 2010.
- [37] B. Steiniger, H. Schwarzbach, and V. Stachniss, “Mikroskopische Anatomie der Zähne und des Parodonts,” p. 15, 2010.
- [38] H. E. Schroeder, “Orale Strukturbiologie,” p. 123, 1982.
- [39] H. E. Schroeder, “Orale Strukturbiologie,” pp. 104–106, 1982.
- [40] D. H. Pashley, “Dentin: a dynamic substrate--a review.,” *Scanning*

- Microsc.*, vol. 3, no. 1, pp. 161–74; discussion 174-6, 1989.
- [41] V. M. Zolotarev and V. N. Grisimov, “Architectonics and optical properties of dentin and dental enamel,” *Opt. i Spektrosk.*, vol. 90, no. 5, pp. 753–759, 2001.
- [42] J. R. Zijp, “Optical properties of dental hard tissues.” pp. 33–40, 2001.
- [43] M. Ehrenfeld, P. Gängler, T. Hoffmann, N. Schwenzer, and B. Willershausen, “Konservierende Zahnheilkunde und Parodontologie,” pp. 43–45, 2010.
- [44] P. K. Upputuri and M. Pramanik, “Recent advances toward preclinical and clinical translation of photoacoustic tomography: a review,” *J. Biomed. Opt.*, vol. 22, no. 4, p. 041006, 2016.
- [45] “Encyclopaedia Britannica,” 2019. [Online]. Available: <https://www.britannica.com/science/refractive-index>. [Accessed: 02-Jun-2019].
- [46] “Physik Cosmos,” 2020. [Online]. Available: <https://physik.cosmos-indirekt.de/Physik-Schule/Brechungsindex>.
- [47] “Filmetrics.” [Online]. Available: <https://www.filmetrics.de/refractive-index-database>.
- [48] P. J. Jeleva and C. G. Parigger, “Photo-acoustic analysis of dental materials and tissue,” vol. 3197616, p. 47, 2005.
- [49] D. Spitzer and J. J. Ten Bosch, “The absorption and scattering of light in bovine and human dental enamel,” *Calcif. Tissue Res.*, vol. 17, no. 2, pp. 133–135, 1975.
- [50] L. V. Wang, “Photoacoustic Imaging and Spectroscopy,” p. 19, 2009.
- [51] F. E. Barber, S. Lees, and R. R. Lobene, “Ultrasonic pulse-echo measurements in teeth,” *Arch. Oral Biol.*, vol. 14, no. 7, pp. 745–760, 1969.
- [52] C. R. Friedrich, “100 Jahre Röntgenstrahlen Erster Nobelpreis für Physik,” *Materwiss. Werksttech.*, vol. 26, no. 11–12, pp. 598–607, 1995.
- [53] E. P. Bertin and E. P. Bertin, “Properties of X-Rays,” *Introd. to X-Ray Spectrom. Anal.*, p. 2, 1978.
- [54] R. Birkner, “Das typische Röntgenbild des Skeletts: Standardbefunde und

- Varietäten vom Erwachsenen und Kind,” pp. 9–11, 2009.
- [55] G. W. Kauffmann, E. Moser, and R. Sauer, “Radiologie,” pp. 19–21, 2006.
- [56] J. Stelzner, “Die Computertomographie als Untersuchungs- und Dokumentationsmethode zur Bearbeitung frühmittelalterlicher Fundkomplexe,” p. 16,24,30, 2016.
- [57] F. A. Pasler and H. Visser, “Taschenatlas der zahnärztlichen Radiologie,” pp. 138–39, 2003.
- [58] W. A. Kalender, *Computertomographie: Grundlagen, Gerätetechnologie, Bildqualität, Anwendungen*, 2nd editio. Publicis, 2006.
- [59] “Bundesamt für Strahlenschutz,” 2019. [Online]. Available: https://www.bfs.de/DE/aktuell/zahl-der-woche/_documents/3-8.html.
- [60] H. L. Möllmann, “Evaluation der Knochenarchitektur im Diät-induzierten Osteoporosemodell der Ratte mittels Mikro-CT,” pp. 8–9, 2016.
- [61] D. C. Hatcher and A. A. Dugoni, “Operational principles for cone-beam computed tomography,” *J. Am. Dent. Assoc.*, 2010.
- [62] D. Rottke, “Digitale Volumentomographie: Was man wissen muss,” *zm-online*, p. 3, 2012.
- [63] M. I. Semper, “Voxeltalk Bildqualität – Voxelgröße [Image Quality – Voxel size],” 2013. [Online]. Available: <https://voxeltalk.wordpress.com/2013/07/18/bildqualitat-voxelgroese-image-quality-voxelsize/>.
- [64] J. G. Fujimoto, C. Pitris, S. A. Boppart, and M. E. Brezinski, “Optical coherence tomography: An emerging technology for biomedical imaging and optical biopsy,” *Neoplasia*, vol. 2, no. 1–2, p. 9, 2000.
- [65] T. L. Szabo, “Diagnostic Ultrasound Imaging: Inside Out,” p. 2, 2014.
- [66] A. M. K. Thomas and A. K. Banerjee, “The History of Radiology,” p. chapter 8 1st page, 2013.
- [67] V. Gibbs, D. Cole, and A. Sassano, “Ultrasound Physics and Technology: How, Why and When,” pp. 39–40, 2009.
- [68] T. X. Misaridis *et al.*, “Potential of coded excitation in medical ultrasound imaging,” *Ultrasonics*, vol. 38, no. 1, pp. 183–189, 2000.
- [69] S. L. Brooks *et al.*, “Imaging of the temporomandibular joint: A position

- paper of the American Academy of Oral and Maxillofacial Radiology,” *Oral Surg. Oral Med. Oral Pathol. Oral Radiol. Endod.*, vol. 83, no. 5, pp. 609–618, 1997.
- [70] L. Jäger, P. Rammelsberg, and M. Reiser, “Bildgebende Diagnostik der Normalanatomie des Temporomandibulargelenks,” *Radiologe*, vol. 41, no. 9, pp. 734–740, 2001.
- [71] M. O. Ahlers, H. A. Jakstat, and A. Hugger, “Klinische Funktionsanalyse: Manuelle Strukturanalyse - Interdisziplinäre Diagnostik.,” pp. 511–542, 2011.
- [72] A. Gahleitner *et al.*, “Die Magnetresonanztomographie in der Dentalradiologie (Dental-MRT),” *Der Radiol.*, vol. 39, no. 12, pp. 1044–1050, 1999.
- [73] D. W. McRobbie, E. A. Moore, M. J. Graves, and M. R. Prince, “MRI from picture to proton,” pp. 79–107, 2017.
- [74] W. A. Fried *et al.*, “Near-IR imaging of cracks in teeth,” *Autho Manuscr. - Proc SPIE Int Soc Opt Eng.*, p. 1, 2014.
- [75] J. F. Arevalo, D. Krivoy, and C. F. Fernandez, “How does optical coherence tomography work? Basic principles,” *Retin. Angiogr. Opt. Coherence Tomogr.*, pp. 217–222, 2009.
- [76] M. Kawasaki, “Optical coherence tomography,” p. 165, 2013.
- [77] J. Welzel, E. Lanckenau, R. Birngruber, and R. Engelhardt, “Optical coherence tomography of the human skin,” *J. Am. Acad. Dermatol.*, vol. 37, no. 6, pp. 958–963, 1997.
- [78] Y. Zhang, “Optical Coherence Tomography guided Laser-Cochleostomy,” pp. 53–55, 2015.
- [79] A. G. Bell and D. Ph, “On the Production and Reproduction of Sound,” *Am. J. Sci.*, vol. 3, no. 20, pp. 305–324, 1880.
- [80] H. Jiang, “Photoacoustic Tomography,” p. 1, 2014.
- [81] G. J. J. Verhoeven and V. Archaeology, “The reflection of two fields – Electromagnetic radiation and its role in (aerial) imaging,” *AARGnews*, no. October, pp. 10–18, 2017.
- [82] M. Brose *et al.*, “Leitfaden „Sichtbare und infrarote Strahlung“,”

- Fachverband für Strahlenschutz e.V.*, p. 6, 2011.
- [83] A. F. Holleman;, N. Wiberg;, and E. Wiberg, "Lehrbuch der anorganischen Chemie," p. 103, 1985.
- [84] iTheraMedical and C. C. Wiest, "iThera Medical Products - MSOT in Vision," 2019. [Online]. Available: <https://www.ithera-medical.com/products/msot-invision/>. [Accessed: 21-Jun-2019].
- [85] J. Xia, J. Yao, and L. Wang, "Photoacoustic tomography: Principles and advances," *Electromagn. waves (Cambridge, Mass.)*, vol. 147, pp. 1–22, 2014.
- [86] S. Sreejith *et al.*, "Near-Infrared Squaraine Dye Encapsulated Micelles for in Vivo Fluorescence and Photoacoustic Bimodal Imaging," *ACS Nano*, vol. 9, no. 6, pp. 5695–5704, 2015.
- [87] BMO Uni Lübeck, "photoacoustics: Breaking through the Optical Diffusion Limit," p. 5532, 2012.
- [88] S. Manohar *et al.*, "Initial results of in vivo non-invasive cancer imaging in the human breast using near-infrared photoacoustics," *Opt. Express*, vol. 15, no. 19, p. 12277, 2007.
- [89] K. Dremel, D. Althoff, A. Hölzing, S. Zabler, and R. Hanke, "MetRIC (Micro and region of interest CT)," *Fraunhofer-Entwicklungszentrum Röntgentechnik EZRT*, p. 1, 2019.
- [90] Dentsply Sirona, "Die 3D-Röntgenfamilie," *brochure*, pp. 18–19, 2020.
- [91] C. Höhne and M. Schmitter, "CAD/CAM supported production process of standardized enamel and dentin tooth discs with different thicknesses for in vitro material testing," *Dent. Mater.*, pp. 1–6, 2020.
- [92] L. Ciocca *et al.*, "Accuracy of fibular sectioning and insertion into a rapid-prototyped bone plate, for mandibular reconstruction using CAD-CAM technology," *J. Cranio-Maxillofacial Surg.*, vol. 43, no. 1, pp. 28–33, 2015.
- [93] J. H. D. Fasel, T. Uldin, P. Vaucher, J. Beinemann, B. Stimec, and K. Schaller, "Evaluating Preoperative Models: A Methodologic Contribution," *World Neurosurg.*, vol. 89, pp. 681–685, 2016.
- [94] E. Huotilainen *et al.*, "Inaccuracies in additive manufactured medical skull models caused by the DICOM to STL conversion process," *J. Cranio-*

- Maxillofacial Surg.*, vol. 42, no. 5, pp. 259–265, 2014.
- [95] J. Janiszewska-Olszowska, K. Tandecka, T. Szatkiewicz, K. Sporniak-Tutak, and K. Grocholewicz, “Three-dimensional quantitative analysis of adhesive remnants and enamel loss resulting from debonding orthodontic molar tubes,” *Head Face Med.*, vol. 10, no. 1, pp. 1–6, 2014.
- [96] C. Von Wilmowsky *et al.*, “A new, highly precise measurement technology for the in vitro evaluation of the accuracy of digital imaging data,” *J. Cranio-Maxillofacial Surg.*, vol. 43, no. 8, pp. 1335–1339, 2015.
- [97] H. Toutenburg, “Deskriptive Statistik: Eine Einführung mit SPSS für Windows mit Übungsaufgaben und Lösungen,” *Springer-Verlag*, pp. 77–78, 2013.
- [98] P. R. Hinton, C. Brownlow, B. Cozens, and I. McMurray, “SPSS Explained,” p. 377, 2004.
- [99] J. Bortz and N. Döring, “Forschungsmethoden und Evaluation,” pp. 27–29, 2006.
- [100] J. Janssen and W. Laatz, “Statistische Datenanalyse mit SPSS für Windows.,” pp. 485–486, 2013.
- [101] J. Bortz, “Statistik,” p. 153f, 2005.
- [102] M. Xu and L. V. Wang, “Analytic explanation of spatial resolution related to bandwidth and detector aperture size in thermoacoustic or photoacoustic reconstruction,” *Phys. Rev. E - Stat. Physics, Plasmas, Fluids, Relat. Interdiscip. Top.*, vol. 67, no. 5, p. 15, 2003.
- [103] R. Cheng, J. Shao, X. Gao, C. Tao, J. Ge, and X. Liu, “Noninvasive Assessment of Early Dental Lesion Using a Dual-Contrast Photoacoustic Tomography,” *Sci. Rep.*, vol. 6, no. February, pp. 2–10, 2016.
- [104] T. Koyama, S. Kakino, and Y. Matsuura, “A Feasibility Study of Photoacoustic Detection of Hidden Dental Caries Using a Fiber-Based Imaging System,” *Appl. Sci.*, vol. 8, no. 4, p. 621, 2018.
- [105] T. Li and R. J. Dewhurst, “Photoacoustic non-destructive evaluation and imaging of caries in dental samples,” *AIP Conf. Proc.*, vol. 29, no. 2010, pp. 1574–1581, 2010.
- [106] Y. H. El-Sharkawy, Y. Badr, M. Gadallah, and A. F. El-Sherif, “Diagnostic

- of human teeth using photoacoustic response,” vol. 6137 61370, no. February 2006, p. 613701, 2006.
- [107] C. Moore *et al.*, “Photoacoustic imaging for monitoring periodontal health: A first human study,” *Photoacoustics*, vol. 12, no. October, pp. 67–74, 2018.
- [108] J. Marotti *et al.*, “Recent advances of ultrasound imaging in dentistry—a review of the literature,” *Oral Surg. Oral Med. Oral Pathol. Oral Radiol.*, vol. 115, no. 6, pp. 819–832, 2013.
- [109] B. Ślak, A. Ambroziak, E. Strumban, and R. G. Maev, “Enamel thickness measurement with a high frequency ultrasonic transducer-based hand-held probe for potential application in the dental veneer placing procedure,” *Acta Bioeng. Biomech.*, vol. 13, no. 1, pp. 65–70, 2011.
- [110] B. Salmon and D. Le Denmat, “Intraoral ultrasonography: Development of a specific high-frequency probe and clinical pilot study,” *Clin. Oral Investig.*, vol. 16, no. 2, p. 643, 2012.
- [111] S. Matalon, O. Feuerstein, and I. Kaffe, “Diagnosis of approximal caries: Bite-wing radiology versus the Ultrasound Caries Detector. An in vitro study,” *Oral Surg. Oral Med. Oral Pathol. Oral Radiol. Endod.*, vol. 95, no. 5, p. 626, 2003.
- [112] B. Kress, A. Gottschalk, M. Schmitter, and K. Sartor, “Benigne Erkrankungen des Unterkiefers im MRT,” *RoFo Fortschritte auf dem Gebiet der Röntgenstrahlen und der Bildgeb. Verfahren*, vol. 176, no. 4, p. 491, 2004.
- [113] B. Kress, Y. Buhl, S. Hähnel, and G. Eggers, “Age- and tooth-related pulp cavity signal intensity changes in healthy teeth : a comparative magnetic resonance imaging,” pp. 2005–2008, 2007.
- [114] K. H. Chan *et al.*, “Clinical monitoring of smooth surface enamel lesions using CP-OCT during nonsurgical intervention,” *Physiol. Behav.*, vol. 176, no. 1, pp. 139–148, 2017.
- [115] Y. Shimada *et al.*, “Noninvasive cross-sectional imaging of proximal caries using swept-source optical coherence tomography (SS-OCT) in vivo,” *J. Biophotonics*, vol. 7, no. 7, pp. 506–513, 2014.

- [116] X. Yang and L. V. Wang, "Monkey brain cortex imaging by photoacoustic tomography," *J. Biomed. Opt.*, vol. 13, no. 4, p. 1, 2008.
- [117] X. Wang, Y. Pang, G. Ku, X. Xie, G. Stoica, and L. V. Wang, "Noninvasive laser-induced photoacoustic tomography for structural and functional in vivo imaging of the brain," *Nat. Biotechnol.*, vol. 21, no. 7, pp. 803–806, 2003.
- [118] I. Steinberg, D. M. Huland, O. Vermesh, H. E. Frostig, W. S. Tummers, and S. S. Gambhir, "Photoacoustic clinical imaging," *Photoacoustics*, vol. 14, no. September 2018, pp. 77–98, 2019.
- [119] R. E. Goldstein, J. L. Nettekville, B. Burkey, and J. E. Johnson, "Implications of follicular neoplasms, atypia, and lesions suspicious for malignancy diagnosed by fine-needle aspiration of thyroid nodules," *Ann. Surg.*, vol. 235, no. 5, pp. 656–664, 2002.
- [120] J. I. Lew, R. A. Snyder, Y. M. Sanchez, and C. C. Solorzano, "Fine needle aspiration of the thyroid: Correlation with final histopathology in a surgical series of 797 patients," *J. Am. Coll. Surg.*, vol. 213, no. 1, pp. 188–194, 2011.
- [121] W. Raber, K. Kaserer, B. Niederle, and H. Vierhapper, "Risk factors for malignancy of thyroid nodules initially identified as follicular neoplasia by fine-needle aspiration: Results of a prospective study of one hundred twenty patients," *Thyroid*, vol. 10, no. 8, pp. 709–712, 2000.
- [122] L. Davies and H. G. Welch, "Thyroid Cancer Survival in the United States," *Arch. Otolaryngol. Neck Surg.*, vol. 136, no. 5, p. 440, 2010.
- [123] M. Toi, K. Inada, H. Suzuki, and T. Tominaga, "Tumor angiogenesis in breast cancer: Its importance as a prognostic indicator and the association with vascular endothelial growth factor expression," *Breast Cancer Res. Treat.*, vol. 36, no. 2, pp. 193–204, 1995.
- [124] L. Smith and S. MacNeil, "State of the art in non-invasive imaging of cutaneous melanoma," *Ski. Res. Technol.*, vol. 17, no. 3, pp. 257–269, 2011.

6.3 Scientific Publications of the Pilot Study

6.3.1 Poster Presentation in Rostock (Germany) 2019



Vergleich der Genauigkeit von photoakustischen Aufnahmen mit einem Micro-CT: In-Vitro Pilotstudie an menschlichen Zähnen

Sonja Schneider¹, Christian Höhne¹, Martin Schneider², Kilian Dremel³, Simon Zabler³, Jan Kloos², Marc Schmitter¹

¹ Proth. Abteilung der Universitätsklinik Würzburg-Bayern, Deutschland

² Eidgenössische Technische Hochschule Zürich, Schweiz

³ Lehrstuhl für Röntgenmikroskopie, Fraunhofer IIS Würzburg, Bayern, Deutschland

Problematik

Für die Bildgebung in der Zahnmedizin wird routinemäßig ionisierende Röntgenstrahlung verwendet. Diese kann direkte oder indirekte Zellschädigungen zur Folge haben.

Dadurch

- ▶ werden die Patienten gerade bei notwendigen Schichtaufnahmen zur Rekonstruktion anatomischer Strukturen verstärkt ionisierender Strahlung ausgesetzt. Dies ist z.B. für die Abklärung des Verlaufs des Nervus mandibularis vor der Implantation oder Exaktion von Zähnen notwendig.
- ▶ ist die bildgebende Diagnostik gerade bei Kindern und Schwangeren stark eingeschränkt.

Aus den genannten Gründen haben wir uns dazu entschlossen die Photoakustik als nicht invasives Verfahren und ihre Umsetzbarkeit in der Zahnmedizin zu untersuchen.

Material und Methoden

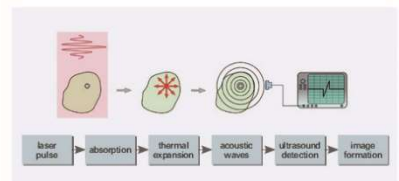
Die für die Pilotstudie verwendeten Zähne (n= 5) wurden mithilfe der Photoakustik (MSOT in Vision) und einem Micro-CT (MetRIC) aufgenommen und in 3D Modelle (3D Slicer) umgerechnet. Beide 3D Rekonstruktionen wurden dann überlagert und die Abweichung der Oberfläche und des Volumens berechnet (GOM).

Ergebnisse

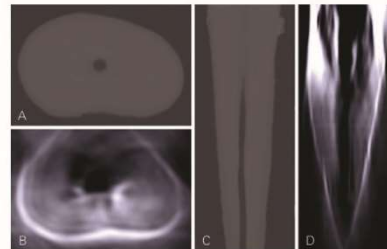
Die Flächenabweichung zwischen Micro-CT und Photoakustik betrug im Mittel $0.05\text{mm} \pm 0.06$, punktuell maximal 0.64mm und minimal -0.54mm . Die Volumenabweichung betrug im Mittel $14.70\% \pm 7.63$, maximal 26% und minimal -4% .

Schlussfolgerung

Im Moment können mit den photoakustischen Aufnahmen Zähne akzeptabel dreidimensional rekonstruiert werden. Es muss jedoch noch die Genauigkeit der Bildgebung erhöht werden.



Das Prinzip der Photoakustik



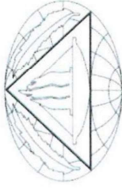
A: Querschnitt des Micro-CT C: Längsschnitt des Micro-CT
B: Querschnitt der Photoakustik D: Längsschnitt der Photoakustik



Micro-CT 3D Modell

Flächenvergleich Photoakustik auf Micro-CT

6.3.2 Oral Presentation in Vancouver (Canada) 2019



IADR

International Association
for Dental Research

VERIFICATION OF ATTENDANCE AND PRESENTATION

The International Association for Dental Research verifies that:

Sonja Jasmin Maria Schneider

attended the 2019 IADR/AADR/CADR General Session & Exhibition
in Vancouver, BC, Canada, June 19-22, 2019, and presented the following research:


**Accuracy of Photoacoustic and MicroCT: Pilot In-Vitro Study in
Human-Teeth**

ADA CERP® | Continuing Education
Recognition Program

The International Association for Dental Research
is an ADA CERP Recognized Provider.

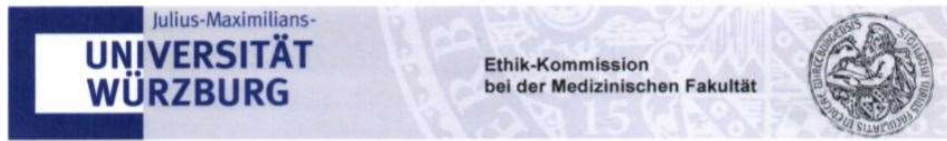
ADA CERP is a service of the American Dental Association to assist dental professionals in identifying quality providers of
dental education. ADA CERP does not approve or endorse individual courses or instructors, nor does it imply
acceptance of credit hours by boards of dentistry.

Concerns or complaints about a CE provider may be directed to the provider or the ADA CERP at www.ada.org/cerp.



Christopher H. Fox, D.M.D., D.M.Sc.
Chief Executive Officer, IADR/AADR

6.4 Ethics Committee Vote



Ethik-Kommission • Versbacher Str. 9 • 97078 Würzburg

Prof. Dr. Gabriel Krastl
Abteilung für Parodontologie
Poliklinik für Zahnerhaltung und Parodontologie
Pleicherwall 2
97070 Würzburg

Ethik-Kommission
Institut für Pharmakologie und Toxikologie
Versbacher Str. 9
97078 Würzburg

Vorsitzende: Prof. i.R. Dr. E.-B. Bröcker
Geschäftsführer: Dr. R. Wölfel
Sekretariat: S. Schmid/ M. Hutter/ A. Geiger
Telefon 0049 (0)931 31 48315
Telefax 0049 (0)931 31 87520
ethikkommission@uni-wuerzburg.de
www.ethik-kommission.medin.uni-wuerzburg.de

Würzburg, 09.02.2015

Unser Zeichen: **15/15** (bitte bei Schriftwechsel angeben)

Beratung nach § 15 Berufsordnung für Ärzte in Bayern

Titel: Simulation der Mundhöhlensituation anhand von Laborstudien unter Verwendung menschlicher extrahierter Zähne.
Antragsteller: Prof. Dr. Gabriel Krastl, Abteilung für Parodontologie, Poliklinik für Zahnerhaltung und Parodontologie, Pleicherwall 2, 97070 Würzburg

Sehr geehrter Herr Prof. Krastl,

die Ethik-Kommission hat Ihren Antrag vom 26.01.2015 auf der Basis der Unterlagen in Anhang 1 geprüft.

Die Ethik-Kommission erhebt **keine Einwände** gegen die Verwendung von auf Grund einer bestehenden klinischen Indikation extrahierten, freiwillig gespendeten und anonymisierten Zähnen von Patienten für den präklinischen Studentenunterricht sowie im Rahmen von Simulationen der Mundhöhlensituation in Laborstudien.

Ggf. sollte man in der Patienteninformation und der **Einwilligungserklärung** noch ergänzen/umformulieren: nachdem der Zahn anonymisiert in der Sammelbox gelandet ist, ist ein Widerruf zwar weiterhin möglich, aber nicht mehr die gezielte Vernichtung gespendeter Zähne. Daher vielleicht "... *Eine Vernichtung der gespendeten Zähne ist nach der Anonymisierung nicht mehr möglich.*"

Mit freundlichen Grüßen

Prof. i.R. Dr. med. Eva-Bettina Bröcker
Vorsitzende der Ethik-Kommission

Ausgefertigt im Auftrag


Dr. med. Reinhard Wölfel
Geschäftsführer

6.5 Informed Consent Form and Patient Information for Extracted Teeth

Universitätsklinikum Würzburg

Zentrum für Zahn-, Mund- und Kiefergesundheit

Poliklinik für Zahnärztliche Prothetik

Direktor: Prof. Dr. M. Schmitter



Poliklinik für Zahnärztliche Prothetik · Pleicherwall 2 · 97070 Würzburg

Einwilligungserklärung

Verwendung von extrahierten Zähnen für Forschung und Lehre

Die schriftliche Patientenaufklärung habe ich erhalten und gelesen. Darüber hinaus bin ich mündlich durch Frau/Herrn _____ aufgeklärt worden.

In diesem Zusammenhang sind mir alle meine Fragen vollständig beantwortet worden. Ich stimme der freiwilligen Teilnahme zu und stelle meinen extrahierten Zahn /extrahierten Zähne für Forschungszwecke und Lehre zur Verfügung. Ich weiß, dass ich meine Zustimmung jederzeit und ohne Begründung und Nachteile für meine weitere medizinische Versorgung widerrufen kann. Eine Vernichtung der gespendeten Zähne ist nach der Anonymisierung nicht mehr möglich.

Unterschrift Patient/gesetzlicher Vormund

Unterschrift Behandler

Universitätsklinikum Würzburg

Zentrum für Zahn-, Mund- und Kiefergesundheit



Poliklinik für Zahnärztliche Prothetik

Direktor: Prof. Dr. M. Schmitter

Poliklinik für Zahnärztliche Prothetik · Pleicherwall 2 · 97070 Würzburg

Patientenaufklärungsbogen über die Verwendung von extrahierten Zähnen für Forschung und Lehre

Sehr geehrte Patientin, sehr geehrter Patient,

vor dem Einsatz neuer Materialien und Behandlungsmethoden müssen zuerst Laboruntersuchungen eine positive Bewertung dieser Materialien und Methoden nachweisen. Um eine möglichst realitätsnahe Simulation der klinischen Situation zu erhalten, werden in der Zahnmedizin extrahierte Zähne in Laboruntersuchungen herangezogen, um verlässliche Aussagen über das Verhalten der unterschiedlichen Materialien oder Versorgungsmethoden in Kombination mit den natürlichen Zähnen treffen zu können.

Zudem ist es im Rahmen der vorklinischen Ausbildung der Studierenden wichtig, dass sie bestimmte Arbeitsschritte an natürlichen Zähnen durchführen können, um dadurch klinische Bedingungen weitestgehend zu simulieren.

Letztlich geht es um die Verbesserung der Behandlung unserer Patienten.

Für Forschung und Lehre benötigen wir extrahierte Zähne. Mit Ihrem Einverständnis verwenden wir Ihre Zähne, die im Rahmen Ihrer Zahnsanierung aus medizinischen Gründen gezogen werden müssen. Es wird **kein unnötiger Eingriff** vorgenommen. Zähne werden nur dann extrahiert, wenn dies medizinisch auch notwendig ist.

Um eine ideale studentische Ausbildung zu gewährleisten und um möglichst realitätsnahe Laboruntersuchungen durchführen zu können, bitten wir Sie, uns den extrahierten Zahn/die extrahierten Zähne zur weiteren Verwendung zu Verfügung zu stellen. Der Zahn/die Zähne würde/-n ansonsten entsorgt werden. Persönlich entstehen dadurch keine Vor- oder Nachteile für Sie.

Für die Patienten die freundlicherweise ihre Zähne zur Verfügung stellen, sind keinerlei unerwünschte Nebenwirkungen zu erwarten. Es erfolgt keine Gewinnung oder Verwertung von genetischen Material.

Ergebnisse der Studien können in Fachzeitschriften, Fachbüchern oder Fachvorträgen veröffentlicht werden.

Ihre Teilnahme erfolgt freiwillig. Sollten Sie mit der Verwendung Ihrer Zähne nicht einverstanden sein, so entstehen Ihnen keinerlei Nachteile hinsichtlich Ihrer weiteren zahnärztlichen Versorgung. Sie haben das Recht Ihre Einwilligungserklärung jederzeit ohne Angabe von Gründen und ohne Nachteile zurückzuziehen.

Für weitere Fragen stehen Ihnen der/die behandelnde Zahnarzt/ -ärztin zur Verfügung.

Vielen Dank für Ihre Unterstützung!

6.6 Acknowledgments

My last remaining task is to acknowledge all the people who contributed to the work described in this thesis. This is an impossible task, given the many people who helped to design, implement, and criticize the work. I am going to try anyway, and if your name is not listed, rest assured that my gratitude is no less than for those listed below.

A few lines are too short to make a complete account of my deep appreciation for my supervisor Prof. Dr. med. dent. Marc Schmitter (Clinical Director of Prosthodontics of the University Hospital of Wuerzburg). His curiosity, dedication, and passion for research impressed and influenced me deeply. His unwavering trust and constant encouragement have been essential to my success over the last two years. I wish to thank him for his steady support in the most difficult times. I want to extend my appreciation for his patience, his full devotion to others, his great understanding, and for the lessons he taught me regarding the importance of details for the success of the photoacoustic project. His contribution has been more than essential for the completion of this thesis.

My deep gratitude goes to Christian Wiest (CEO at iThera Medical GmbH in Munich, Germany) and Katja Haedicke (Application Specialist at iThera Medical GmbH in Munich, Germany) who gave me permission to use the MSOT inVision 256-TF and invested plenty of time and passion to help me to get the most out of the photoacoustic images and answered every question I had.

Special thanks go also to Dr. rer. nat. Simon Zabler (Postdoc of the Institute for X-ray Microscopy, Fraunhofer IIS in Wuerzburg, Germany) and his team Dr. rer. nat. Kilian Dremel and M.Sc. Daniel Althoff who gave permission to use all required equipment and provided enthusiastic help and training on MetRIC. It was an unforgettable experience to work with them.

This acknowledgments section would not be complete without mentioning my team Dr. Julian Boldt, Tamer Kurum, Lisa Kanus, Sarah Krumpa, Dr. Daniel Hellmann, Dr. Kirsten Probst, Dr. Engelke Rasche, Sören Rehling, Franziska Rösner, Raphael Schwarzbauer, Enrico Webelhorst, and Dr. Anna Winter. And Theresa Schaad. All of them helped me to collect the needed teeth and always

gave advice and support whenever they could. It was a particular pleasure to work with them. Grateful acknowledgment goes especially to Dr. Christian Höhne and Axel Schurig. Both helped me with all their experience to analyze the data and supported me throughout the whole time.

A really important person I also want to show my deep gratitude to is Katharina Zemljanskij. She offered me great advice concerning all image rights issues and design questions.

And I also want to thank a special person: Prof. Dr. Dr. Erich Wintermantel. He always supported me on my research project by hook or by crook! Whether it was just a simple conversation about research or to give me advice about writing my dissertation.

Finally, I wish to thank my parents for their love and patience during the past 28 years. My parents have always prioritized my education and raised me to set high goals for myself. They taught me to value honesty, courage, and humility above all other virtues. I have always needed to work hard to achieve my goals in life, and they have always been there for me as an unwavering support. I would like to dedicate this thesis to them and thank them with all my heart for their love, care, and patience.

And special gratitude goes to my brother PhD Dr. Martin Schneider (postdoc at Stanford University). My apprentice pursuit into the world of science would not have been the same without his approach to research and science. He always took me on his research projects whenever I had the chance to visit him. He was the one who introduced me to the principle of photoacoustics and investigated all his passion and time to teach his little sister how to become part of the world of science.